Investigation and Simulation of Ion Flow Control over a Flat Plate and Compressor Cascade

Andrew Capers Thompson

Thesis submitted to the faculty of the Virginia Polytechnic Institute and State University in partial fulfillment of the requirements for the degree of

Master of Science

In

Mechanical Engineering

Committee:

Walter O'Brien, Chair

William Cousins

Mark Paul

May 13, 2009

Blacksburg, VA

Keywords: Active Flow Control, Plasma, Corona Discharge, Separation, Compressor Cascade, Boundary Layer Transition

Investigation and Simulation of Ion Flow Control over a Flat Plate and Compressor Cascade

Andrew Capers Thompson

ABSTRACT

An investigation of ion flow control was performed to determine the effect of a positive, DC corona discharge on the boundary layer profile along a flat plate and to examine its ability to prevent separated flow in a low-speed compressor cascade. Flat plate tests were performed for two electrode configurations at free-stream velocity magnitudes of 2.5, 5, 7.5, and 10 m/s. Boundary layer velocity profile data was taken to measure the performance of the electrode pairs. Ion flow control was also tested in the compressor cascade for a stagger angle of 25° at angles of attack equal to 6° and 12°. The cascade tests were performed at free-stream velocities of 5 and 10 m/s. Static tap data was used to characterize separated flow behavior and the effect of ion flow control on flow reattachment. A computational model was developed using the commercial CFD software Fluent. This model simulates ion flow control as a body force applied to the flow through user-defined functions.

The study showed that the corona discharge has the ability to increase near-wall velocities and reduce the thickness of the boundary layer for flow over a flat plate. Ion flow control successfully prevented trailing edge separation in a compressor cascade for angles of attack of 6° and 12°; however, the flow control scheme was not able to prevent leading edge separation for angle of attack equal to 12°. The ion flow control CFD model accurately predicted flow behavior for both the flat plate and cascade experiments. The numerical model was able to simulate the boundary layer velocity profiles for flat plate tests with good accuracy, and was also able to predict the flow behavior over a compressor blade. The model was able to show the trends of separated and reattached flow over the blade surface.

Acknowledgements

First, I would like to thank Dr. Walter O'Brien for taking me on as a graduate student during my first semester at Virginia Tech. I went to meet with him after the first week of his class and he told me about all of the exciting proposals he had submitted that could lead to new projects for his research group. I asked him to be my advisor and he accepted; promising to find funding for me during the next semester through one of his upcoming projects. I got more than I bargained for; however, when he pitched the idea of plasma flow control. The last three years have been a wild ride, but I have gained an amazing wealth of knowledge on a subject that I might have never thought twice about under the guidance of any other advisor. Thank you for your support, guidance, and motivation.

I'd like to thank Dr. Cousins and Pratt & Whitney for funding me during my extended stay in graduate school. Hopefully this thesis and the results within provide a useful foundation for an emerging research topic at this university. Thanks to Dr. Paul for serving as both an instructor and committee member.

Thank you to the members of the Virginia Tech Turbo Lab, especially Matthew Perry and Daniel Villarreal. Vincenzo was not only a colleague that I could always count on to provide cromulent research advice and embiggen my engineering knowledge, but also a friend and roommate that helped me to survive the last three years. Dan was always willing to lend a helping hand in the lab, and I would have gone stir crazy without the musical entertainment he provided daily. Also, those two were founding members of airport roof days, a great stress reliever when times got tough. Other Turbo Lab members that need thanking are Darius Sanders, who helped me to develop my Fluent model; Michael Perry, who taught me the ins-and-outs of the VT Low-Speed Wind Tunnel; and Gautham Ramakrishna, who aided in the care and calibration of the instrumentation in the test cell.

I'd like to thank Trey Bolchoz for his friendship and help over the past 4 years. I never could have made it out of undergrad without him and graduate school would have eaten me alive if I had to go it alone. Thanks to Jordan Farina for bringing true Southern heritage to southwest Virginia. No one else knows that when someone asks you if you're a god, you say "YES"! And thanks to all my other friends who provided both support and distractions, and for knowing which of the two was truly better for me.

Thank you to my family. All of you have provided emotional (and financial) support during my academic career and I would have never been able to accomplish this much without you. I am truly thankful to have so many people that believe in me despite the fact that they have no idea what I've been doing in school for the past seven years. Thanks to the LBD, Bosco Thompson. Nothing wipes away the stress of a tough day like a circle wag when you walk through the front door.

Last but not least, I'd like to thank Dr. Jaci Moon. You may have never understood what I was ranting about at the end of each day, but you listened and nodded along just as well. If I was experimentin' at the airport or designing graph paper on the computer, you always wanted to hear about it. You were always the best distraction that came along right when I needed one.

Table of Contents

List of Figures

List of Tables

Notation

α^* - Angle of attack of compressor cascade blade

ξ – Stagger angle of compressor cascade

$C_{ps,\ blade}$ – Dimensionless static pressure coefficient, blade surface

P_{s1} – Static pressure measured at the wind tunnel calibration section

P_{sb} – Static pressure measured at tap along blade surface

P_{t1} – Total pressure measure at the wind tunnel calibration section

U – Free-stream velocity magnitude

k – Turbulent kinetic energy

k_L – Laminar kinetic energy

ω – Specific dissipation rate

y+ - Non-dimensional wall distance

u_t – Friction velocity

y – Distance to the first grid node

ν – Kinematic viscosity

ρ – Density of the free-stream air

τ_w – Wall shear stress

F_p – Plasma-induced body force

ρ_c – Local positive ion charge density

E – Local electric field strength

J – Current density

K – Positive ion mobility

Chapter 1

Introduction

There are various forms of active flow control used to prevent boundary layer separation. For example, air can be blown through surface holes to reenergize the boundary layer and maintain attached flow. Conversely, surface holes can be used to suck off the boundary layer and provide undisturbed flow. The obvious advantages of flow control are drag and inlet flow distortion reduction. However, in gas turbine engines, compressor bleed air must be used for some of these control schemes. This robs the engine of potential mass flow that can be used to drive the turbine. There is interest, therefore, in active flow control schemes that do not require bleed air. Ion flow control provides such a solution.

Often referred to in literature as "electric wind", "ionic wind", "electrohydrodynamic (EHD) flow", or "electroaerodynamics," ion flow control involves the application of an electrostatic body force to the air stream using two electrodes driven by a voltage source. An upstream, positive electrode ionizes the incoming air through the emission of a large electric field. The positive ions are then attracted to the downstream electrode, being at ground or negative potential, and, through molecular bombardment, impart a body force to the neutral air molecules. The force is directed downstream and towards the surface, and, with enough magnitude, can affect boundary layer shape and reattach the flow.

1.1 Motivation

The following work was performed in order to develop a foundation for ion flow control research at the Turbomachinery Laboratory of the Virginia Tech Mechanical Engineering Department. Active flow control through corona discharge is an emerging technology that has gained popularity over the past decade; however, it is a new technology to the members of the Turbo Lab. In order to guide this fundamental study, a non-dimensional analysis was performed to understand the design space of ion flow control and provide guidance in the initial investigation of the phenomenon. Along with establishing ion flow

control techniques that build on previous plasma physics studies, the development of a simple, coupled computational model to guide future research was desired. Therefore, various flat plate experiments were conducted to validate the developed CFD model that may be used to design future experiments for the Turbo Lab group. With future work in mind, a test was also performed to examine the effects of ion flow control on preventing separated flow in a low-speed compressor cascade.

1.2 Background and Previous Research

Research has been conducted on several types of plasma actuators, which involve both alternating and direct current supply voltages. In some cases, AC or DC voltage pulses, on the order of a few micro- or nanoseconds, are applied to the electrodes instead of operating the actuator at a constant voltage level. Other variations in the actuation process involve alternative electrode designs and configurations. Ion flow control is used in applications where maintaining a laminar flow regime is desired, transitional flows are expected, or boundary layer separation is causing severe system losses. This includes, but is not limited to; low pressure turbine blades, oscillating airfoils, and aircraft wing surfaces. The use of plasma actuation for compressor blades is ideal, but, because of the adverse pressure gradient, the force needed to reattach the flow would require large power consumption. Current research has been devoted to maximizing the efficiency of electrode design, configuration, and operating mode in order to increase the amount of force created by the electrode pair.

1.2.1 Ion Flow Control Principles – Kinetic Theory of Gases and Ion Mobility

A fundamental study of ion flow control begins with an investigation of gaseous conductors and discharge physics. Classical electrical engineering texts were a good source for learning the basics of the kinetic theory of gases and the movement of ions through an electric field, two subjects at the fundamental core of ion flow control.

Howatson [1], in a 1976 introductory text on gas discharges, thoroughly outlines the three types of steady state gas discharges: the Townshend or dark discharge, the glow discharge, and the arc discharge. The three types are differentiated by the amount of

current each carries. Howatson goes on to discuss mean free paths and gas particle collisions. One type of collision discussed is the class of inelastic collisions in which charge transfer takes place. Charge transfer is the collision of an ion and a neutral molecule in which positive charge is exchanged, and it can lead to inaccurate values of calculated mobility if the ions are under the influence of an electric field. Howatson defined the drift velocity for ions in the presence of an electric field and the effect of ion mobility on the current density. These theoretical values; however, required assumptions on the number of molecules in the affected region and the ratio of positive to negative ions produced by electric field emission. He detailed the two key functions of electrodes within a gas discharge, to initiate the discharge and to provide charged particles in maintaining it.

Another source for fundamental electrical theory is Raizer's [2] 1991 text on gas discharge physics. He discussed basic topics that were covered by Howatson, such as drift velocity, ion mobility, and current density; however, Raizer provided more experimental results to validate theoretical derivations. Raizer provided validated equations for current and charge density in weakly and strongly ionized plasmas, detailing the relationships between gas discharge physics and the governing equations for fluid motion. He applied the continuity equation for plasmas in an external electric field where there is a measurable current that under steady-state conditions would have no source.

1.2.2 Direct Current Corona Discharge

Cobine [3] is an electrical engineering text from 1941 that outlined the elementary principles of both gaseous conductors and discharge physics. He not only provided an introduction to the kinetic theory of gases, but also provided the necessary theory behind glow discharge formation. While Cobine provided similar information on kinetic theory as Howatson and Raizer, he more thoroughly investigated the corona discharge. He stated that when the air gap between two parallel electrodes is increased, a distance is reached at which the gas breaks down at a voltage less than the spark-breakdown voltage for that gap length. The resulting breakdown is referred to as a glow discharge. At

atmospheric pressure the glow discharge is given the name "corona." The corona discharge appears as a bluish-white cloud sheathing the positive electrode with the negative electrode possessing equally spaced reddish tufts along its length. Corona may be created using DC or AC voltage supplies, with the AC corona exhibiting alternating positive and negative corona emission behavior on the electrode pair, based on the current cycle. Cobine also tells us that onset voltage for gas breakdown is not dependent on electrode spacing and is a function of the radius of curvature of the emitting electrode. He distinguished between the formation of positive and negative corona discharges, which are categorized by the polarity of ions generated. The critical electric field gradient necessary to generate a positive corona in air is lower than the critical gradient for negative corona. Cobine also stated that for wires with a diameter greater than 0.075 mm, a positive corona discharge appears before negative corona, while for wires of a smaller diameter the opposite is true. He provided plots of voltage-current relationships for atmospheric discharges and the expected current range, on the order of several milliamps, for positive and negative corona. As stated above, Howatson and Raizer did not provide much discussion on the corona discharge, other than to classify it amongst the other gaseous conductors and discuss corona losses in high-voltage power lines [1, 2]. Raizer did, however, discuss time scales for breakdown and the concept of streamer theory [2]. He stated that streamer theory was based on the concept of thin ionized channels, or streamers, growing between the electrodes on paths left by electron avalanches resulting in a breakdown [2]. These breakdowns due to large electric fields created through the use of dielectric materials are important in later discussions on increasing the efficiency of electrode configurations.

Leger et al. [4] tested the formation of corona discharge for various electrode configurations. They used not only parallel copper wire electrodes, but also thin (13 μm) aluminum plating as the downstream anode. Leger operated the electrode pair at opposing polarities, with the upstream electrode above ground potential and the downstream at a negative bias. One unique aspect of the work done by Leger et al. was the categorization of so-called corona discharge "regimes." Because electrode configuration and atmospheric conditions influenced the voltage-current relationship of

the discharge, Leger described the physical appearance and behavior of the corona as the electric field is increased, identifying five definitive classifications. These different operating regimes for the discharges were both quantitatively and qualitatively classified. Operating envelopes for different discharge types were given current and power consumption ranges. Also, the appearances of the corona types were described based on emission spectra and location of the ionized sheath within the electric field. For each discharge type, Leger et al. also commented on the stability of the corona. This is of importance when operating the electrode pair for extended periods. Leger et al. also performed tests at different relative air humidity levels. As expected, current values increased for lower humidity levels and the discharge became more unstable when humidity levels increased.

1.2.3 Effect of Ion Flow Control on Boundary Layer Growth and Separation along a Flat Plate

In another paper by the research group comprising Leger et al. [5], the preliminary findings of their initial investigation were expanded to encompass the theory behind corona discharges and the effect on flow along a flat plate. For parallel wire electrode configurations, the group measured induced near-wall velocities as a function of corona current as well as static pressures along the flat plate. Consideration was given to the efficiency of the DC corona discharge actuators (a small percentage) and the reduction in drag caused by electrohydrodynamic (EHD) actuation. Boundary layer measurements were performed for free-stream velocities of 5 and 10 meters per second and showed a measurable increase in near-wall velocities. Pressure measurements and drag reduction calculations were performed for velocities up to 25 m/s.

Walker [6] performed flat plate tests using DC corona discharge along a flat plate for free-stream velocities ranging from approximately 3 m/s to 18 m/s. The study featured fine diameter (0.05 mm) copper wire for the upstream positive electrode with a 13 mm wide by 0.3 mm thick stainless steel shim stock electrode spaced 2.54 mm downstream. Although referred to as a “negative” electrode throughout the paper, the downstream electrode remained at ground potential during tests. Boundary layer measurements were

taken immediately downstream of the rear electrode and for all cases the boundary layer profile exhibited a reversed flow phenomenon. This suggests the presence of a negative corona discharge. Although this was hypothesized by Walker and the cause linked to a smaller radius of curvature on the downstream electrode, the true culprit can be determined through the fundamental teachings of Cobine [3]. The positive electrode used by Walker measured 0.05 mm in diameter and was exhibiting negative ionic emission for all applied voltages. Walker examined the effects of using multiple "stages" of electrode pairs in an attempt to magnify the force produced by the ion flow. Each stage beyond the initial electrode pair exhibited alternate polarity from the previous pair to continuously pull along the ionized fluid. This "megastaging," as Walker referred to it, in fact increased the effectiveness of the corona discharge; however, the negative corona induced velocities in opposition to the free-stream, effectively "thickening" the boundary layer. These undesirable results led to an inconclusive study.

Rickard et al. [7] also investigated methods of using stages of electrodes to maximize ionic flows. Rickard examined the theory behind generating the maximum current density for point corona discharges. Experimenting with such techniques, Rickard was able to double ion-induced velocities through circular orifices when 7 stages were employed.

Seraudie et al. [8] performed flat plate tests based on actuator characteristics similar to those of Leger et al. [4, 5]. Using flush mounted as well as embedded electrodes, they measured boundary layer profiles at free-stream velocities of 5 and 10 meters per second. With glass pitot-tube instrumentation, Seraudie was able to measure near wall velocities in the region between electrodes, with maximum velocities of 4 to 5 m/s reached for the flush mounted electrode pair. Other than providing inter-electrode measurements, Seraudie also demonstrated similar results to those of Leger et al. [5].

During preliminary tests, all sources experimenting with corona discharge [4, 5, 6, 7, 8] were able to recreate steady state results. However, the repeatability of experimental results was only achieved when atmospheric conditions were controlled and electrodes

were kept free of non-uniformities. This meant that the relative humidity and temperature must be controlled in the testing facility. Also, Rickard et al. [7] reported a reduction in day-to-day variability of results when the laboratory was outfitted with a continuously operating dehumidifier. The repeatability of results is important for a flow phenomenon to be accurately modeled.

1.2.4 Effect of Ion Flow Control on Airfoil Separation

As free-stream velocities increase above the range of 10 meters per second, many researchers move from the DC corona discharge to the AC or pulsed-DC actuated single dielectric barrier discharge (SDBD). This plasma actuator consists of two plate electrodes separated by a dielectric material. The result is a reduction in the current produced by the discharge, but also a stronger electric field producing a larger ion cloud. This reduction in current along with the short duty cycle of the voltage pulse leads to lower power consumption. There is also a dynamic effect due to the pulsed nature of the discharge, which more effectively increases the momentum transfer in the near-wall region.

Roupassov et al. [9] determined that the SDBD actuator, when operated at nanosecond pulse widths, can control boundary layer separation, lift and drag coefficients, and reduce noise for a Mach number range of 0.05 to 0.85. Roupassov measured near zero values for ion-induced velocities for SDBD actuators, proving that the physical mechanism for enhanced boundary layer control was different from that of DC corona discharges. Shock waves and secondary vortex flows due to nanosecond pulse disturbances cause a "transversal momentum transfer" in the boundary layer region that prevents separation. Roupassov states that the main mechanism for flow reattachment is the "energy transfer to and heating of the near-surface gas layer." Expanding on fundamentals explained by Raizer [2], Roupassov investigated the streamer discharge as a case for creating strong electric field gradients and ionization waves. Roupassov claims that the propagation of streamers from the positive to ground electrode causes the initial shock wave and thermalization of near wall gases. There is a secondary discharge as the accumulated

charge on the ground electrode travels back to the positive electrode as the initial pulse drops below the ground charge value; resulting in a second pressure wave that further enhances the efficiency of the actuator.

Wall et al. [10] conducted an experimental study that investigated the reattachment of separated flow for a highly loaded turbine blade. They used a pulsed DC DBD plasma actuator at pulse rates of 25, 50, 75, and 100 pulses per second. The voltage and pulse width were held constant to set a nominal level of power consumption per pulse. Wall et al. comment on the overall power consumption reduction by employing pulsed DC actuators versus alternating current powered DBD's. Using phase-locked particle image velocimetry (PIV), results for a Reynolds number of 23,500 saw a 39% decrease in the separation region for a pulse frequency of 100 Hertz.

Corke and Post [11] examined the effects of AC SDBD plasma actuators on flow separation in various applications. They showed that the lift-to-drag ratio could be increased by up to 400% when an actuator is placed at the leading edge of a wing at a large angle of attack. Trailing edge separated flow from a "Pak B" low pressure turbine (LPT) blade was prevented by placing an actuator at mid-chord. Corke and Post experimented with a type of "pulsed" AC operation by supplying voltage to the actuator in a short duty cycle. They found that periodic actuation was more effective than steady operation for the flow applications examined.

Huang et al. [12] performed a series of experiments that examined the effects of SDBD plasma actuators in a LPT cascade. Huang used the same SDBD actuator configuration as Corke and Post for Pak B blades. Huang et al. developed baseline results for Reynolds numbers ranging from 10,000 to 100,000 and observed a separation point located at 70% chord. The separated region was shown to be reduced when the blades were fitted with vortex generating "tabs." These results were then compared to the effect that SDBD actuators had on the separation region. The effectiveness of the plasma actuator was similar to that of the tab vortex generators; as they both reduced the separation region towards the trailing edge of the airfoil. Unlike the tabs, the SDBD actuator is used only

when the flow exhibits separated behavior and do not cause an increase in drag when not in use.

Rivir et al. [13] compared the voltage-current characteristics of plasma actuators powered by alternating and direct current sources. The AC frequency was varied from 2 to 15 kHz and the DC pulse widths ranged from 22 nanoseconds to 2 microseconds. The AC source required large current values relative to the DC pulse actuator. Higher electrode voltages and peak power levels were achieved by the pulsed DC actuator. PIV measurements were taken in the near-wall region that showed an increase in local velocities up to 250%. These experiments were run for low free-stream velocities (3 to 5 m/s). Rivir et al. also performed infrared measurements of the plasma discharge and found temperatures within the actuator-affected region of 315 °C. They suggested that this drastic increase in near-wall temperature was an important physical mechanism in the effectiveness of SDBD actuators.

1.2.5 Modeling Ion Flow Control

El-Khabiry and Colver [14] performed a purely numerical analysis of drag reduction through DC corona discharge for low speed flows over a flat plate. The numerical model simulated the formation of a corona discharge between two parallel wire electrodes. The gas phase conservation of charge, Poisson's equation of electrostatics and the conservation of charge at a solid interface were the partial differential equations used to model the transfer of charge and the conversion of electrical energy to mechanical motion. The above equations were combined with the boundary layer equations for two-dimensional, incompressible steady flow. The electrostatic equations were coupled with the equations of motion through a body force term. El-Khabiry and Colver used empirical breakdown and current-voltage relationships developed by other researchers to model the corona discharge. The deposition and removal of charges from surrounding surfaces was included in their numerical solver, and determined that for a grounded downstream electrode increased charge is lost to the surroundings. Also, their model included the conduction and convection terms for determining the current density. For experiments performed at Reynolds numbers below 100,000, El-Khabiry and Colver

observed a thinning of the boundary layer due to corona discharge as well as a reduction in the drag. Other results included an increase in effectiveness when the gap length between electrodes was reduced. Although no experimental results were given to validate the numerical model, El-Khabiry and Colver cited agreement with experimental trends of other researchers despite a slight over-prediction of drag reduction.

Boeuf et al. [15] developed a two-dimensional fluid model to show that the force on the flow that is generated by a DBD is of the same physical mechanism as the ionic wind force observed for corona discharges. Boeuf's numerical model was developed through complex gas discharge physics theory which was reduced by various assumptions proven through experimental work. The model simulated an AC DBD for voltage peaks of 5 to 20 kV at frequencies ranging from 1 to 10 kHz. Rather than simulating the effects of the DBD on a particular flow field, Boeuf et al. modeled the discharge dynamics and the force produced by the actuator in ambient air. They have proven that the electrohydrodynamic force for an SDBD is due to momentum transfer from ions to neutral molecules. This is a result of a large ionic region created above the surface of the discharge. A succession of high current and low current pulses is generated by the surface discharge with the force being the largest during the low current phase. During the low current phase, the large ionic cloud is formed and spreads above the dielectric surface.

The stance of Boeuf et al. on the physical mechanism behind ion flow control is in contrast to the findings of Roupassov et al. [9] discussed in the previous section. The understanding of this technology is in its nascent stages and this is most clearly evident when reviewing a wide range of literature on the subject. The conflicting views demonstrate the need for further research to develop more accurate methods of modeling plasma flow control. The research group led by Roupassov developed their own numerical model that, like Boeuf, concentrated on the discharge dynamics and formation of the ionization cloud due to pulsed excitation. Roupassov modeled a pulsed DC SDBD and used streamer propagation theory, taken from the findings of Raizer [2], to simulate the electric field distribution created by the plasma actuator.

Rizzetta and Visbal [16] performed a three-dimensional numerical investigation of SDBD flow control for transitional flow over an LPT blade. The computational model developed for this study differs from those in previous research in the way that the plasma-induced body force is coupled to the equations of fluid motion. El-Khabiry and Colver used equations of electrostatics and charge conservation to evaluate the ionic force through finite differencing schemes. This force was then coupled to the boundary layer equations through a body force term. Rizzetta and Visbal employed a simplified method in which the body force term was represented by a "plasma scale parameter" found through the non-dimensionalization of the governing equations. This parameter represented the ratio of electrical to inertial forces and was applied based on the gradient of electric pressure. Rizzetta and Visbal performed no experiments to determine the value of this parameter; however, the magnitude was calculated based on previously published research. The goal of their study was to develop a more practical plasma model that allowed for complex flow fields to be solved while still simulating the ion induced body force with some accuracy. Simulations were run for both continuous and pulsed plasma actuation, and results showed that pulsed excitation had a greater effect on preventing separation. Rizzetta and Visbal also examined the effect of counter-flow plasma actuation, in which the force was directed upstream, and determined that it provided the most effective control when pulsed. However, continuous counter-flow actuation was less effective in preventing separation at the trailing edge of the blade. The efforts of Rizzetta and Visbal lend credence to the work of Boeuf et al. [15], which featured a similar ion-induced body force term in modeling plasma actuation.

1.3 Summary and Organization

After thoroughly examining the fundamentals of gaseous discharges and the ion flow control research performed over the past decade, the knowledge gained was used to determine the scope of the proposed research. Based on the resources available to the Virginia Tech Turbo Lab, work began on the foundation of ion flow technology. As a research group approaching a new technology, an emphasis was placed on a fundamental understanding and basis for developing new applications for the technology, always with

future research in mind. We decided to investigate DC corona discharges on a flat plate and on compressor blades in a cascade, and to develop appropriate models for the two flow applications.

The following document details the development of ion flow control research at Virginia Tech's Turbo Lab. First, the experimental setup and methodology are explored to inform the reader of the techniques and practices employed in this research along with a description of the facility and equipment used to conduct tests. Next, the experimental design, procedures, and results are given. The next section details the development of the computational model. The fifth section contains the comparison of the experimental data to the numerical results. Finally, the conclusion contains the author's suggestions and recommendations for continuing research. Supplemental information, such as plasma formation techniques and a study of non-dimensional ion flow control parameters are included in the appendices.

Chapter 2

Experimental Setup and Methodology

This chapter describes the facilities and equipment used to perform experiments for this research. Also discussed are the techniques employed to calibrate the instrumentation necessary to conduct tests.

2.1 High Voltage Power Supplies

The direct current corona discharge was driven by a Glassman High Voltage Power Supply Model FC30P4. The unit is capable of supplying 30 kilovolts at a current of 4 milliamps. Voltage and current levels are set using dials on the unit's front panel, and the supply automatically switches between constant-current or constant-voltage regulation based on load discharge. This protects the unit against overloads and arcs. It also provides the option of operating at set electric field strengths or at a desired current value. The high voltage power supply came equipped with voltage and current readouts on the front panel. The set voltage value and corresponding current, or vice versa, could be measured in this way. Readout values of voltage were accurate to 0.5% of reading +2% rated voltage. The accuracy of the current monitor was 1% of reading +0.05% rated.

Initial plasma characteristic tests and literature review led to the desire for a second power supply that would deliver high voltage at a negative potential. Supplying one electrode with a negative high voltage creates a preferred path for positive ions generated by the upstream, positive-biased electrode, thus eliminating charge losses to the surroundings [14]. A Pacific Instruments Model 204-10 High Voltage Power Supply was found within the Virginia Tech Mechanical Engineering Department. It is capable of producing 2,010 Volts below ground potential at a maximum current of 10 milliamps. The output is continuously adjustable within the operating range of the supply; however, for experiments conducted in this study the supply was set to – 2 kilovolts. The supply is fitted with a front panel meter that displays output voltage and current with accuracy up to 2%.

2.2 Wind Tunnel

The flat plate and compressor cascade experiments were performed at the Turbomachinery Laboratory located at the Virginia Tech/Montgomery County Executive Airport. The open-return wind tunnel used in these experiments was designed and constructed in the 1980's by former graduate students of the Turbo Lab. It is shown below in Figure 2.2.1, which is taken from the thesis of Michael Perry [17].

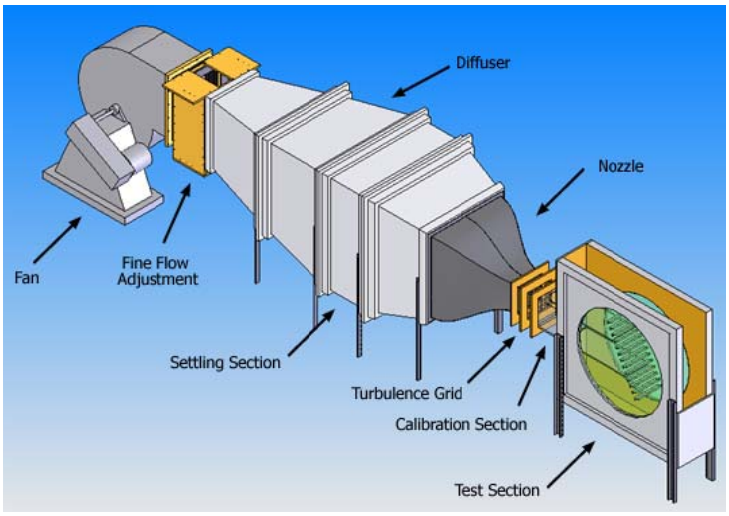

Figure 2.2.1 Computer model of the VT Low-Speed Wind Tunnel with cascade test section attached [17]

Flow through the tunnel is supplied by a centrifugal fan powered by a 15 horsepower electric motor. Tunnel speed is governed by guide vanes at the fan's inlet. A wooden fixture situated between the fan outlet and the diffusing section of the tunnel allows for finer flow speed adjustments by opening two sliding baffles to bleed off air. Screens may also be placed into the wooden fixture to create a flow blockage that reduces the free-stream velocity at the wind tunnel exit. At its lowest setting, the tunnel Reynolds number based on compressor blade chord length could be reduced to around 7,500, or a velocity magnitude of approximately two meters per second. A Reynolds number of around 200,000, or velocity magnitude of approximately thirty five meters per second, can be reached by removing the screens, closing the baffles, and opening the fan's inlet guide vanes [17].

The wind tunnel comprises three major components. The first part is a diffusing section that contains honeycomb screens that provide flow uniformity and reduce free-stream turbulence levels [17]. Following the diffuser is a settling section with a 48" square cross section. Finally, a two-section nozzle provides a 16:1 contraction ratio to the 12" square cross section exit of the wind tunnel [17]. A wooden flange at the nozzle exit is used to attach the calibration section where the tunnel's exit velocity is set [17]. Either the flat plate test platform or cascade test section can be placed at the 12" square cross section exit of the calibration section. Further description of the flat plate and cascade test assemblies is provided below.

2.3 Flat Plate Test Platform

The test platform used to conduct all flat plate experiments was assembled from available materials at the Turbo Lab. A wooden frame was used as the support structure for the flat plate, which was constructed from a 0.5 cm thick sheet of polycarbonate plastic that measured 46 cm wide by 57 cm long. The frame supported the flat plate at a height of 1.13 meters, the vertical centerline of the wind tunnel's exit nozzle. During testing, the flat plate was positioned squarely against the exit of the calibration section of the wind tunnel. The purpose of these tests was to measure boundary layer growth along the flat plate and the effect of the corona discharge on the velocity profile in the near-wall region. In order to measure velocity, a boundary layer probe was constructed that allowed data to be taken at various stream-wise locations.

2.3.1 Boundary Layer Probe

The boundary layer probe designed for these experiments consisted of a pitot probe capable of measuring the total pressure, and static taps along the plate to determine the static pressure at a given stream-wise position. The difference in these two values gave the dynamic pressure. The static taps were placed every 2.54 centimeters starting at 2.54 centimeters from the leading edge of the flat plate. Figure 2.3.1 shows the location of the static taps along the plate.

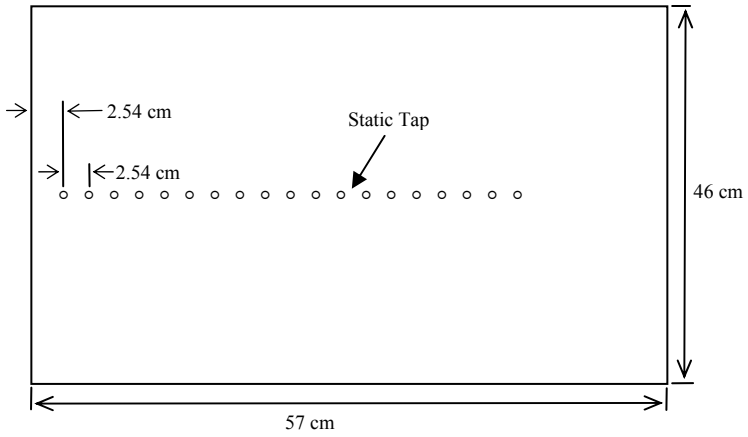

Figure 2.3.1 Location of static taps along the flat plate

An apparatus was constructed that allowed the pitot probe to be moved to the proper stream-wise position, aligning the tip of the probe with the static tap at the desired measurement location. This positioning device featured a threaded traverse so that the probe could be raised to specified distances above the plate surface and as such measure the velocity profile. The pitot probe is 1.6 mm in diameter and traverses the flow in 0.75 mm increments. The boundary layer probe and flat plate are shown below in Figure 2.3.2.

Figure 2.3.2 Picture of boundary layer positioning apparatus mounted above flat plate

2.4 Cascade Test Section

The cascade test section used in this research has been in service at the VT Turbo Lab for several decades. It consists of a linear cascade used to test axial flow compressor airfoils. Over the years it has been modified to meet the requirements of various research projects. Most recently, it was used in a parametric study of free-stream turbulence effects on separation at low Reynolds number for the thesis of Michael Perry [17]. A more detailed discussion of the cascade test section can be found in Perry's thesis and it is from this document that the cascade and blade geometries summarized below are taken.

2.4.1 Cascade Geometry

The test section is constructed from two Plexiglas circles, 1.37 meters in diameter, which are bolted to the blades that separate them. When fastened in this manner, the discs create a solid rotating row of blades. Guide boards are placed upstream of the blade row to maintain the same cross sectional area exiting the calibration section of the wind tunnel. Downstream of the blades, tailboards are placed at the same angle as the blades to continue this area to the exit of the cascade. The two pictures below show the cascade test section and the linear blade row.

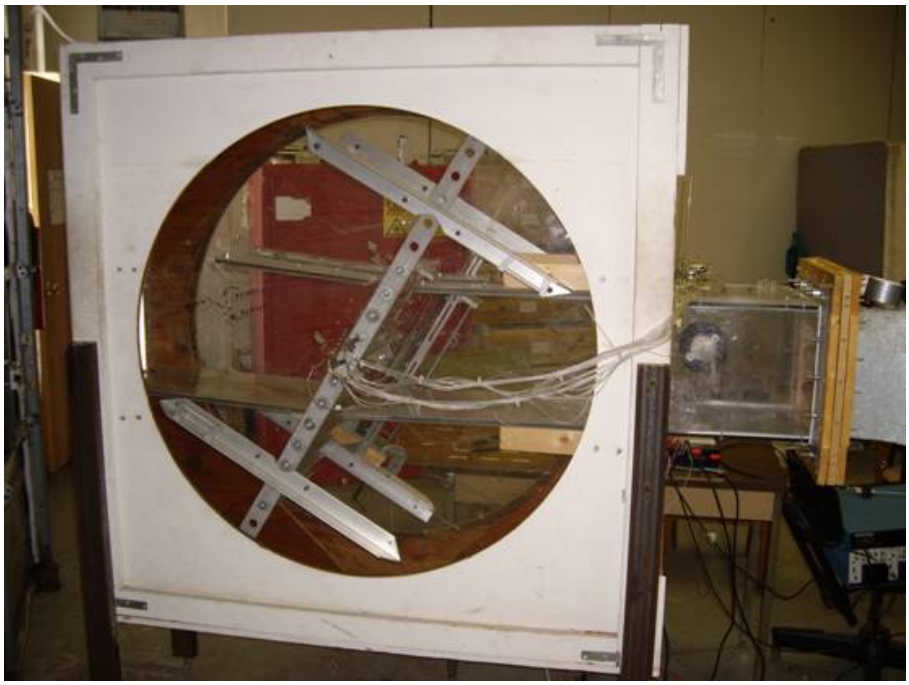

Figure 2.4.1 Cascade test section attached to calibration section at exit of wind tunnel

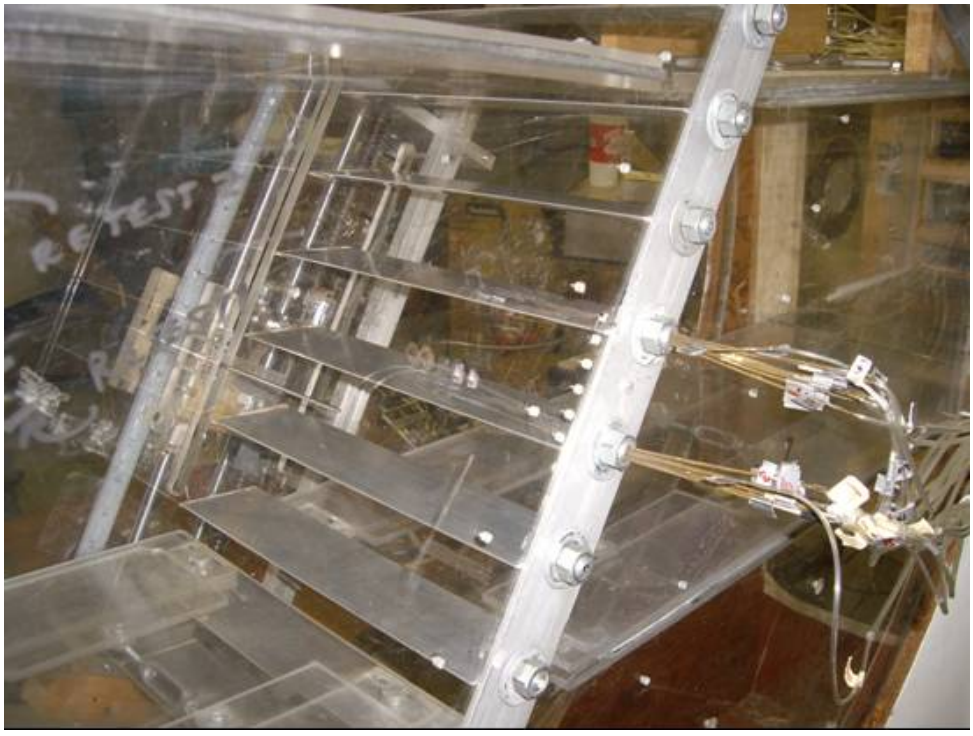

Figure 2.4.2 Linear blade row bolted to Plexiglas circles that make up the cascade test section; surface pressure measurement connections are shown

2.4.2 Blade Geometry

The compressor blades used in this study were based on an airfoil geometry with a flat pressure surface and semi-circular suction surface. The stagger angle of the blades is set by rotating them about the bolts which secure them to the test section. Once secure, the desired angle of attack is achieved by rotating the solid assembly of blades within the wooden test section housing to the proper setting. The blade geometry is shown in Figure 2.4.3.

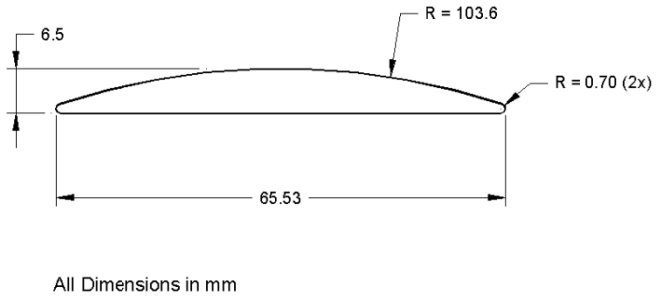

Figure 2.4.3 Dimensions of cascade blades used for experimentation [17]

The blade span is approximately 300 mm and the blade spacing is equal to the chord length, resulting in a cascade solidity of 1.00.

2.4.3 Static Pressure Taps

Static taps are placed along the surfaces of the two center blades at increments along the chord length. Figure 2.4.4 shows the chord stations were the taps are located.

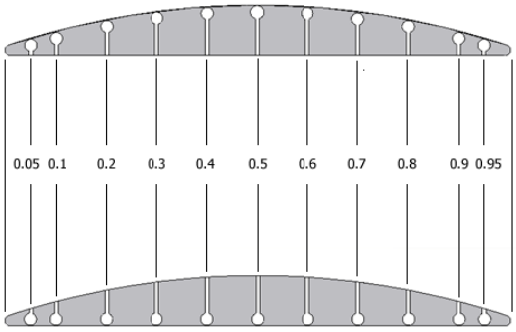

Figure 2.4.4 Static pressure tap locations by fraction of chord [17]

The taps are used to characterize the behavior of the flow along the blade surface. The static pressure due to airflow over a blade is impressed upon the surface itself [17]. Static taps can measure these surface pressures and allow us to determine whether the airflow above a tap location is separated.

2.5 Pressure Measurements

In order to measure boundary layer velocity profiles and cascade performance, accurate pressure measurements were essential in this research. The low velocities and small pressure variations required transducers that were very accurate for small pressure differentials. Also, precise care was used in calibrating the transducers at regular intervals throughout the research. The necessary equipment to maintain accurate measurements were already in place thanks to prior efforts by former colleagues.

2.5.1 Pressure Transducers

All pressure measurements were taken with three Setra Model 264 Very Low Differential Pressure Transducers. The ranges of the transducers were 2.5" H_2O, 0.5" H_2O, and 0.1" H_2O, and came with calibration certified accuracies of ±0.25% of full scale. Error associated with the accuracy of the transducers was calculated in the thesis of Michael Perry [17]. The transducers were regularly calibrated throughout the duration of this research and were found to maintain the proper range.

2.5.2 Calibration Point Detector

The device used to calibrate the Setra pressure transducers was a Dwyer Model 1430 Microtector Electronic Point Gage, which has an accuracy of ±0.00025" H_2O over a range of 0 to 2" H_2O. The Microtector is certified as traceable to a National Institute of Standards and Technology master. It is capable of measuring positive, negative, or differential pressures over its operating range. The gage determines pressures in the same way as a manometer, but has a current running through the fluid columns. When the point probe is lowered into contact with the water level, the circuit is completed and the

current meter engages, allowing the pressure to be read off of the micrometer. As stated above, weekly calibrations were performed to ensure accuracy of pressure measurements.

2.6 Data Acquisition

A National Instruments DAQCard-6062E PCMCIA card along with LabVIEW software was used for data acquisition. Analog inputs with a 12 bit resolution were used. The sampling rate was varied depending on the type of measurement being taken. During flat plate tests, a sampling frequency of 1 kS/s was used. For wake measurements during cascade testing a much higher sampling rate was required. In keeping with the testing methodologies of Perry [17], the rate was increased to 500 kS/s. National Instruments documentation lists the absolute accuracy of the analog inputs as ± 17.945 mV. Perry's [17] error analysis included this accuracy specification.

Chapter 3

The Experiment; Design, Procedure and Results

This chapter outlines the experimental process and presents the results of the research performed on ion flow control. Electrode pair design and configuration are important in the production of an efficient and stable corona discharge. Therefore, the first series of tests that were performed investigated the characteristics of corona discharges for various electrode types and arrangements. After determining the two most effective electrode pairs, flat plate experiments were carried out to measure the effect of corona discharge on the boundary layer profiles. Finally, an electrode pair was fitted to an instrumented blade in the cascade test section to determine the effect of ion flow control on preventing separation. These experiments were guided by a non-dimensional analysis that can be found in detail in Appendix A1.

3.1 Plasma Characteristics

Inspired by gaseous discharge fundamentals in Cobine [3] and investigative studies by previous researchers such as Leger et al. [4], a characterization of plasma formation was undertaken as the first experimental step in this study. Various electrode geometries and configurations were examined for maximizing current flows and determining the most stable operating range for positive, DC corona discharges. A voltage-current relationship was determined for each electrode pair and important data trends, such as current density, onset electric field strength, power consumption, and arc breakdown voltage were calculated to compare the effectiveness of each pair. From these tests, the two most efficient electrode designs were chosen and used in flat plate and cascade experiments.

3.1.1 Electrode Configurations

A direct current, positive corona discharge was selected for the ion flow control flat plate tests. This was the desired configuration because it would ensure a lower power consumption discharge with the plasma force applied in the stream-wise direction. To

ensure the stability of the positive corona discharge, only wires with diameter greater than 0.075 mm were used as positive electrodes, for reasons discussed above [3].

Three electrode types were selected that included AWG 34 gage copper wire with a diameter of 0.16 mm, AWG 22 gage copper wire with a diameter equal to 0.645 mm, and copper foil that measured 5 mm in width and was 0.1 mm thick. These were chosen because they provided the opportunity to test electrodes of different shape and emission radii, as well as pair electrodes with different geometries to study the effect on corona stability. Table 3.1.1 below shows the combinations of electrode type used in each arrangement along with the name given to each configuration.

Table 3.1.1 Electrode configurations and designated names

Configuration Name	Positive Electrode	Ground Electrode
34-34	AWG 34 copper wire	AWG 34 copper wire
34-22	AWG 34 copper wire	AWG 22 copper wire
34-foil	AWG 34 copper wire	Copper foil
22-34	AWG 22 copper wire	AWG 34 copper wire
22-22	AWG 22 copper wire	AWG 22 copper wire
22-foil	AWG 22 copper wire	Copper foil
Foil-34	Copper foil	AWG 34 copper wire
Foil-22	Copper foil	AWG 22 copper wire
Foil-foil	Copper foil	Copper foil

The electrodes were mounted flush to the plate surface and tested at different gap lengths. For each electrode pair, tests were performed at gap lengths of 1, 2, 3, and 4 centimeters. This meant that for all nine configurations four gap lengths were tested for a total of thirty-six plasma characteristic tests. Figure 3.1.1 below depicts all nine electrode arrangements. The upstream (left) electrode is designated as (+) for positive and the downstream (right) electrode as (g) for ground.

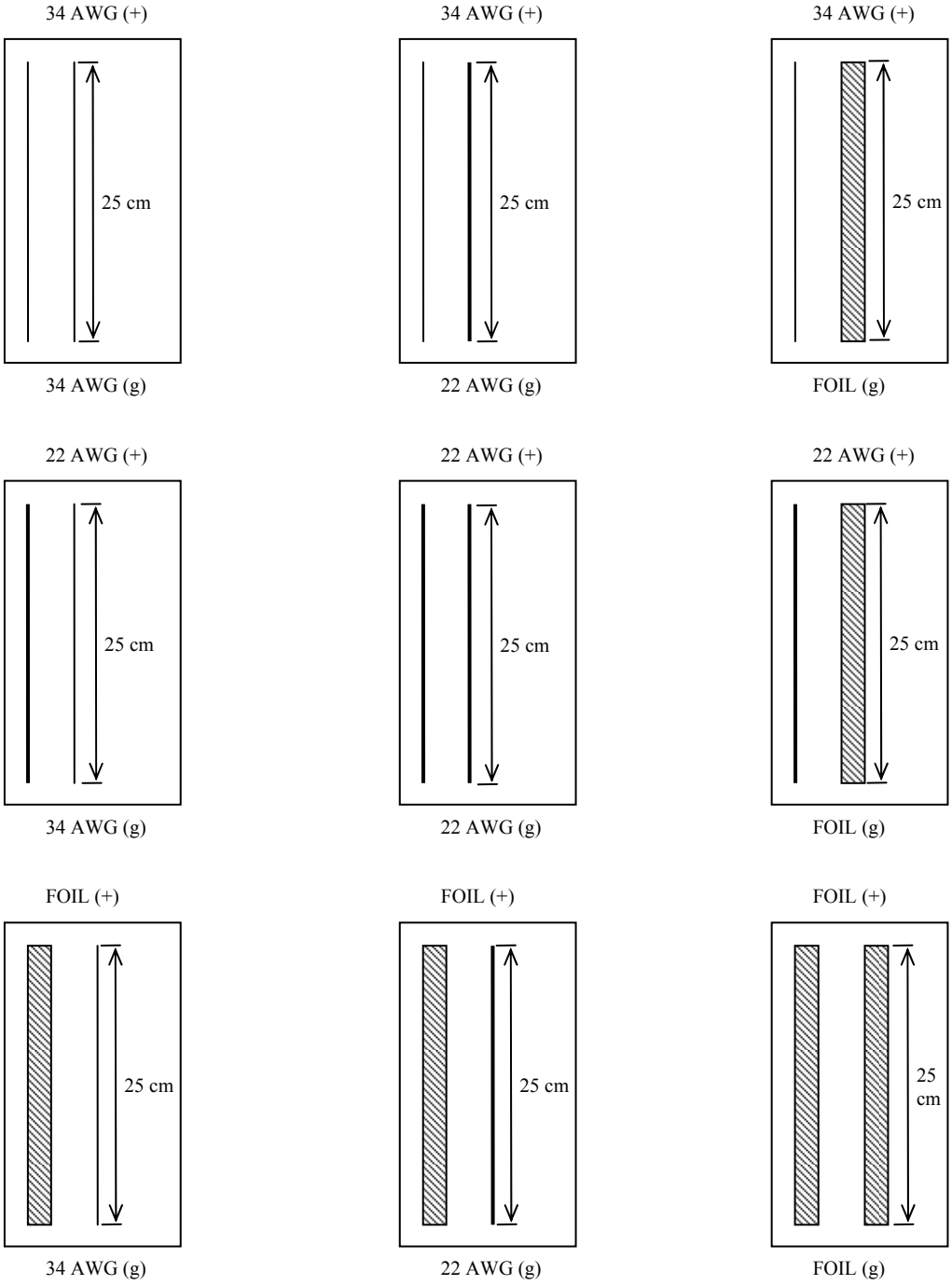

Fig 3.1.1 Arrangement of electrodes for all nine configurations tested

For the plasma characteristics tests, each setup was designated by the electrode type in the upstream and downstream position as well as the spacing between electrodes. Therefore, a setup given the name "34-foil-2" featured the AWG 34 copper wire as the

positive electrode, the copper foil as the ground electrode, and was arranged at a gap length of 2 centimeters.

3.1.2 Voltage-Current Characterization

As outlined above, nine electrode configurations were tested at four gap lengths. For each experiment, the current setting was adjusted on the high voltage power supply and the voltage required to generate that current was measured. The results of these tests are given below in three plots. The plots are organized by the positive electrode for that set of configurations. The current per unit length of electrode is plotted versus the electric field strength. The field strength was calculated by dividing the voltage potential by the electrode gap length. Measurements were only taken for stable corona discharges; therefore, the first data point on each plot represents the onset voltage for that pair and the last data point is the arc breakdown voltage. The results for the nine configurations are shown in Figures 3.1.2 through 3.1.4.

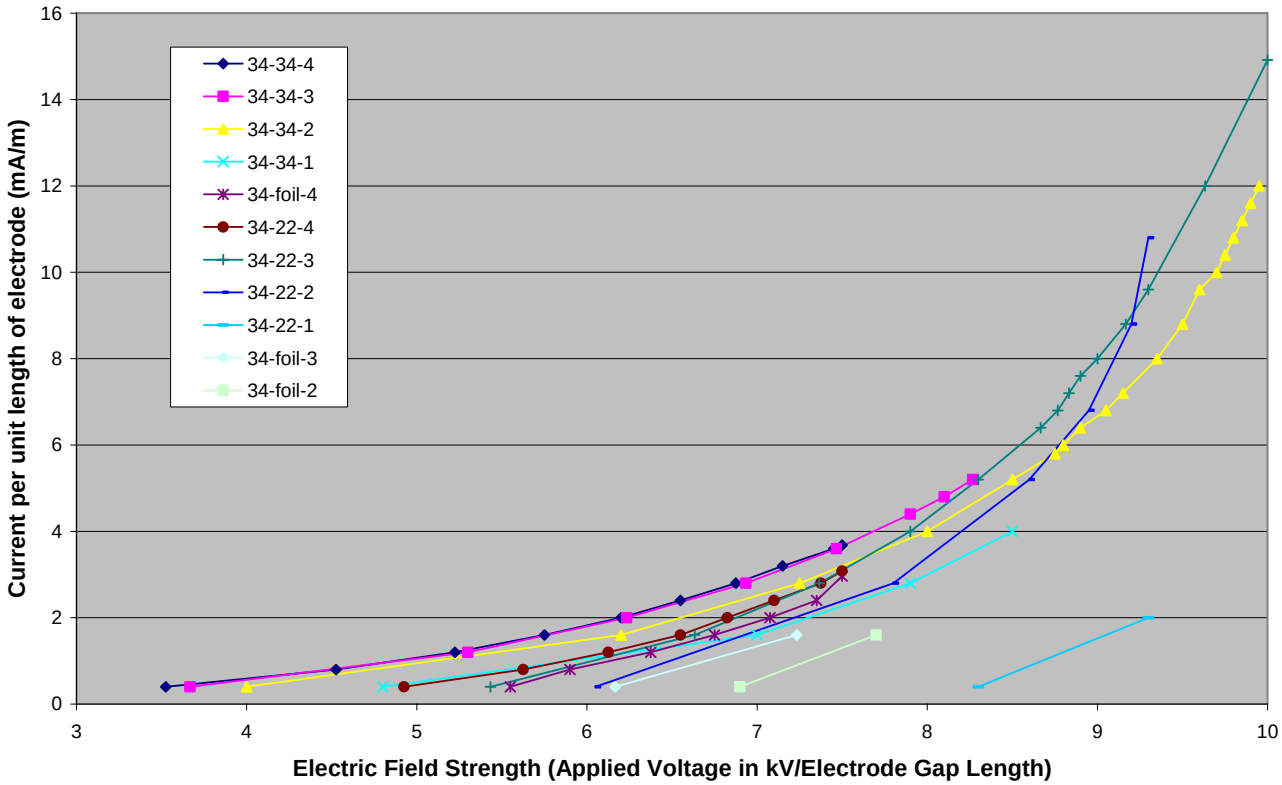

Figure 3.1.2 Current per unit length of electrode versus electric field strength for electrode configurations 34-34, 34-22, and 34-foil

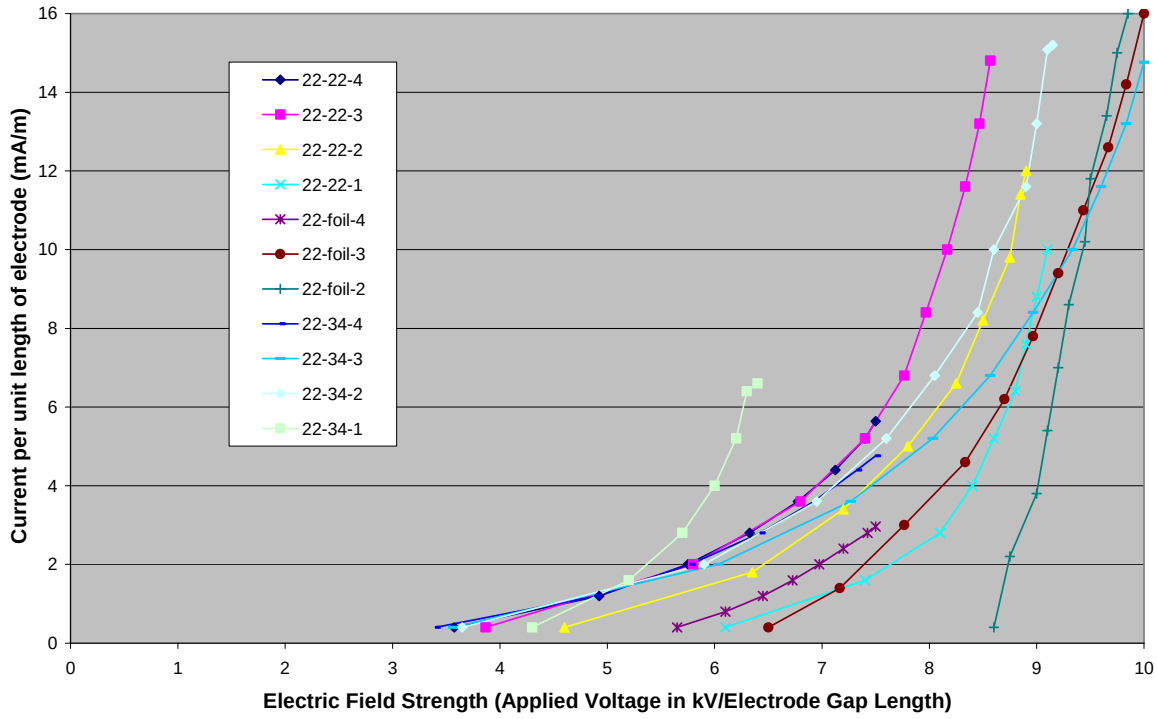

Figure 3.1.3 Current per unit length of electrode versus electric field strength for electrode configurations 22-34, 22-22, and 22-foil

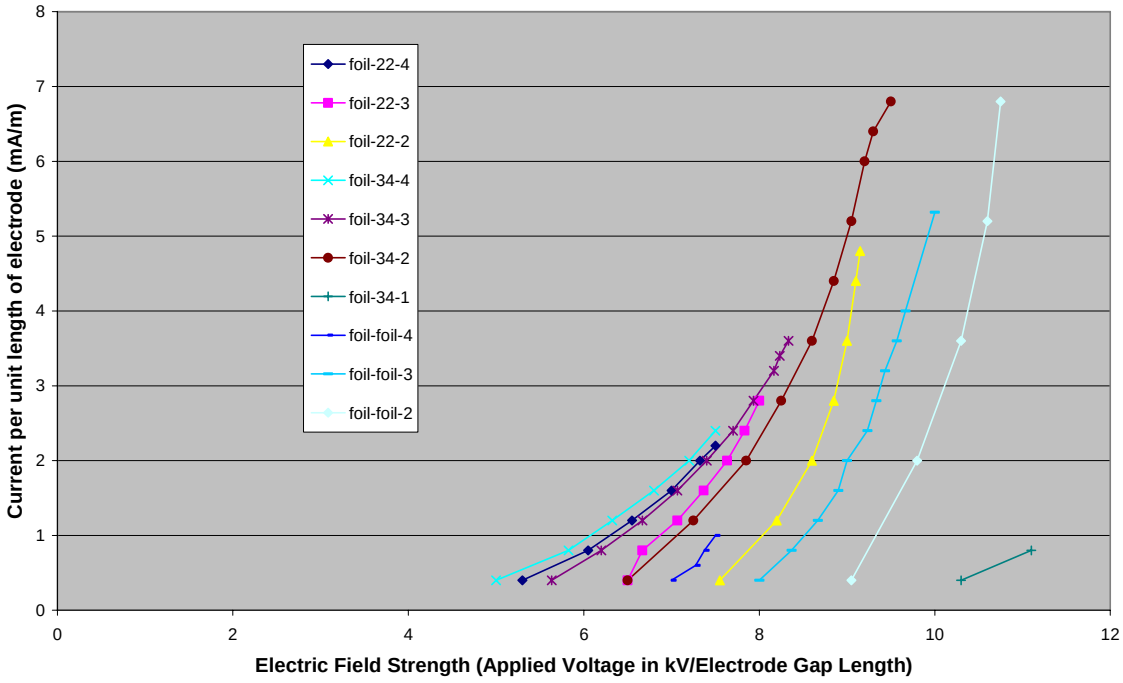

Figure 3.1.4 Current per unit length of electrode versus electric field strength for electrode configurations foil-34, foil-22, and foil-foil

Electrode pairs that exhibited the most stable behavior featured a low onset voltage and produced measurable current for a wide range of applied voltage. Configurations with the AWG 34 copper wire positive electrode demonstrated the lowest discharge onset voltages as well as the widest operating range. The AWG 22 positive electrode configurations produced the greatest current values. Not only did the copper foil positive electrode set require the largest onset voltage, but they also produced the smallest amount of current. All configurations in which the positive electrode consisted of copper wire produced more stable corona discharge as the operating points of these pairs covered a wider range of applied voltage potentials.

Another important characteristic of the emitter/receptor design was the amount of power required to produce optimum current values. To compare the power consumption of the configurations, the power per unit length of electrode was plotted versus the current per unit length of electrode. Figures 3.1.5 through 3.1.7 contain the power comparisons for the nine electrode pairs.

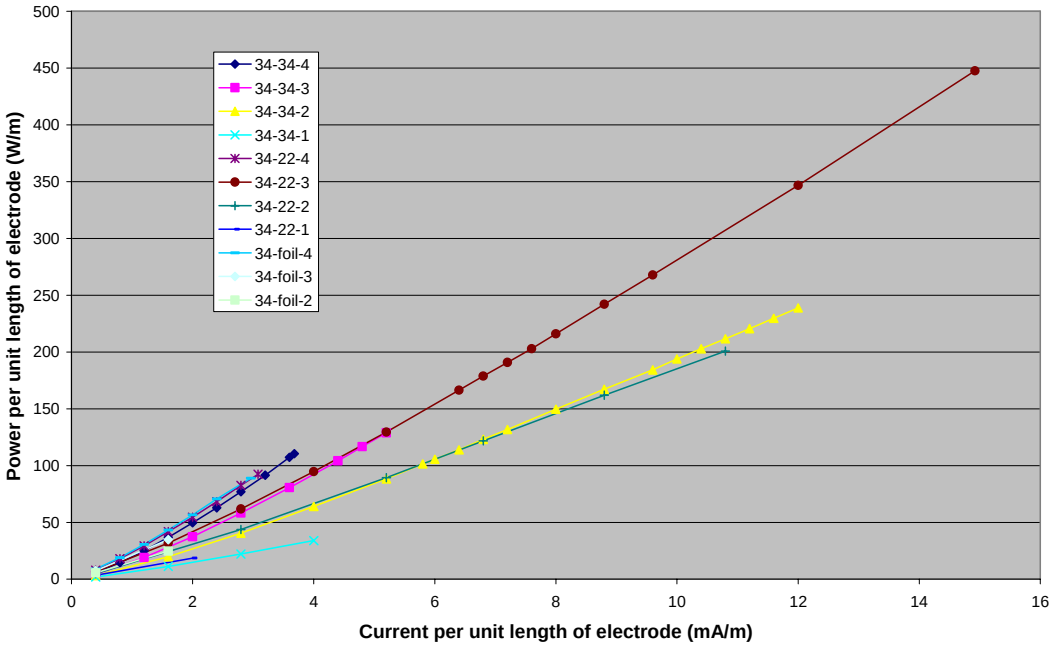

Figure 3.1.5 Power per unit length of electrode versus current per unit length of electrode for electrode configurations 34-34, 34-22, and 34-foil

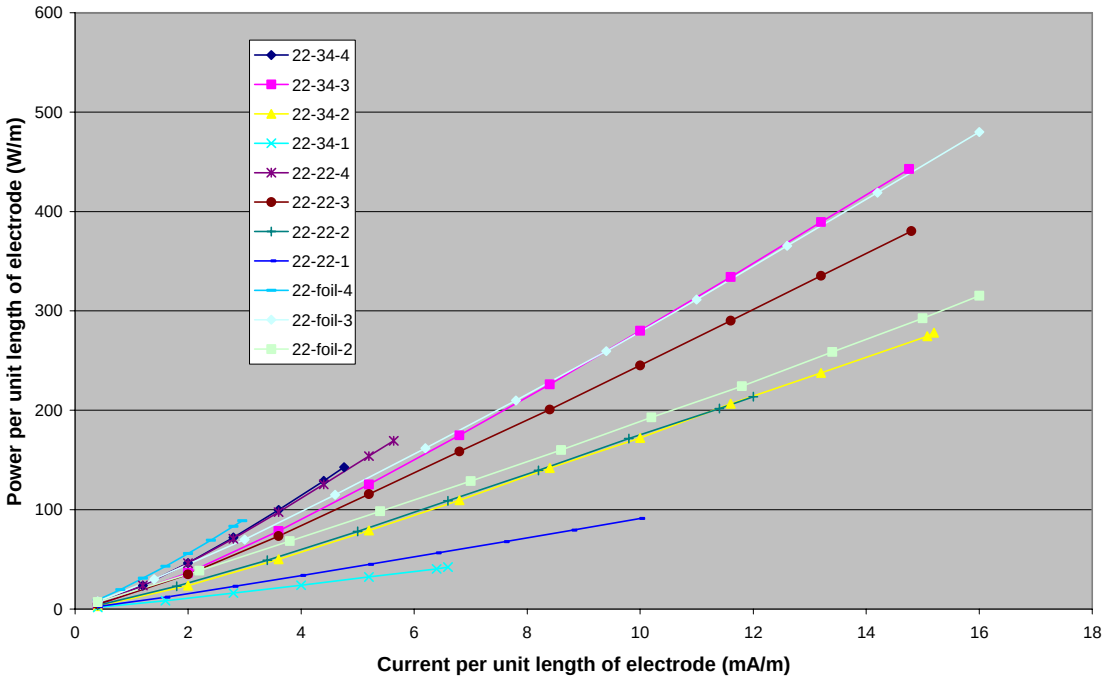

Figure 3.1.6 Power per unit length of electrode versus current per unit length of electrode for electrode configurations 22-34, 22-22, and 22-foil

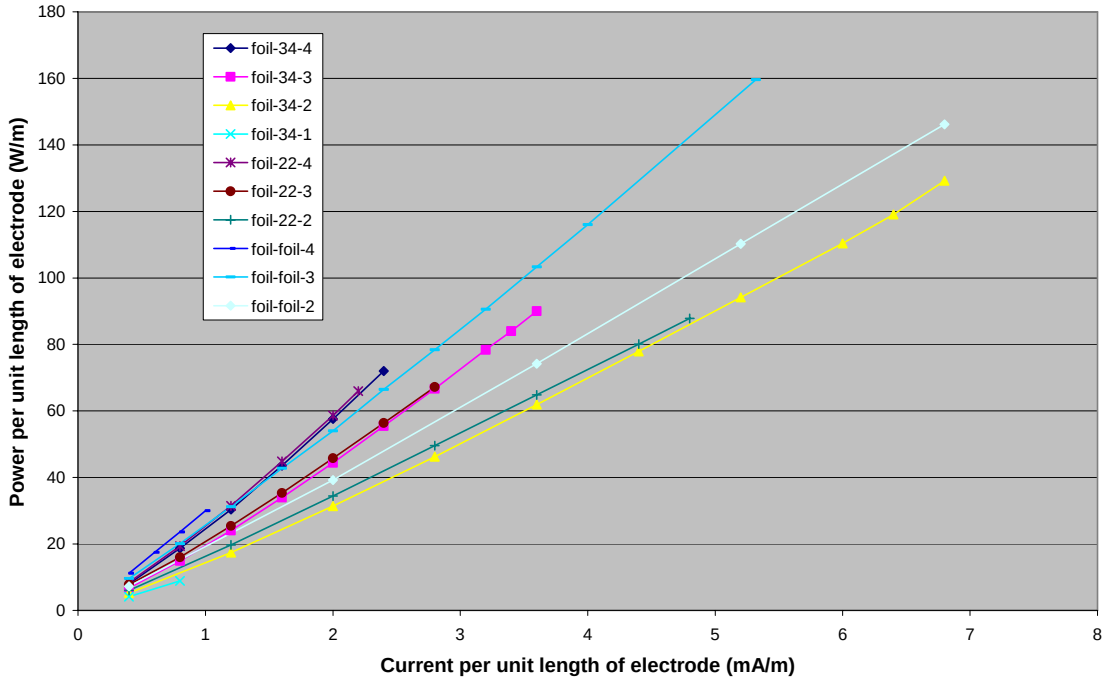

Figure 3.1.7 Power per unit length of electrode versus current per unit length of electrode for electrode configurations foil-34, foil-22, and foil-foil

The important feature of these plots is for an electrode pair to produce a large amount of current for a limited consumption of power; therefore, data trends in the lower-right portion of the plotted area were desirable. As expected, less power was required to produce a given current for shorter electrode gap lengths. For the AWG 34 copper wire positive electrode cases, there was a significant decrease in power consumption for a reduction in electrode spacing. The AWG 22 positive electrode set, however, showed the largest reduction in power requirement for decreasing gap lengths. A large reduction in power consumption for decreasing gap length was not observed for electrode configurations consisting of the copper foil as the positive electrode.

3.1.3 Electrode Pair Selection

The most important criterion for determining the most effective electrode pairs was the maximum amount of current produced. For those configurations exhibiting large currents, the pairs that were able to produce that current at lower power consumption levels were chosen. Also, the stability of the discharge was of importance. It was necessary that the corona exist within a wide operating range and maintain its discharge current for a variety of atmospheric conditions.

Based on the above criteria and the results presented in the previous section, the selected electrode configurations were the 34-22-3 and 22-foil-2 setups. They are shown below in Figure 3.1.8.

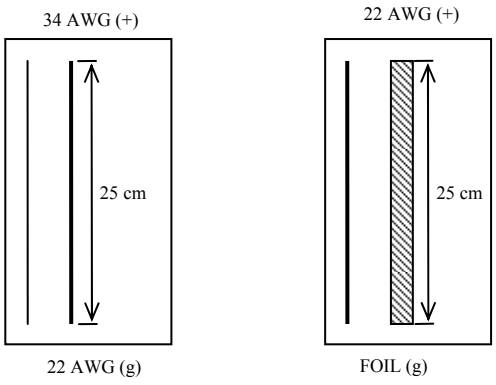

Figure 3.1.8 Selected electrode configurations: 34-22-3 and 22-foil-2

The current-voltage characteristics of the two configurations are plotted in Figure 3.1.9 and the power requirements of each are compared in Figure 3.1.10.

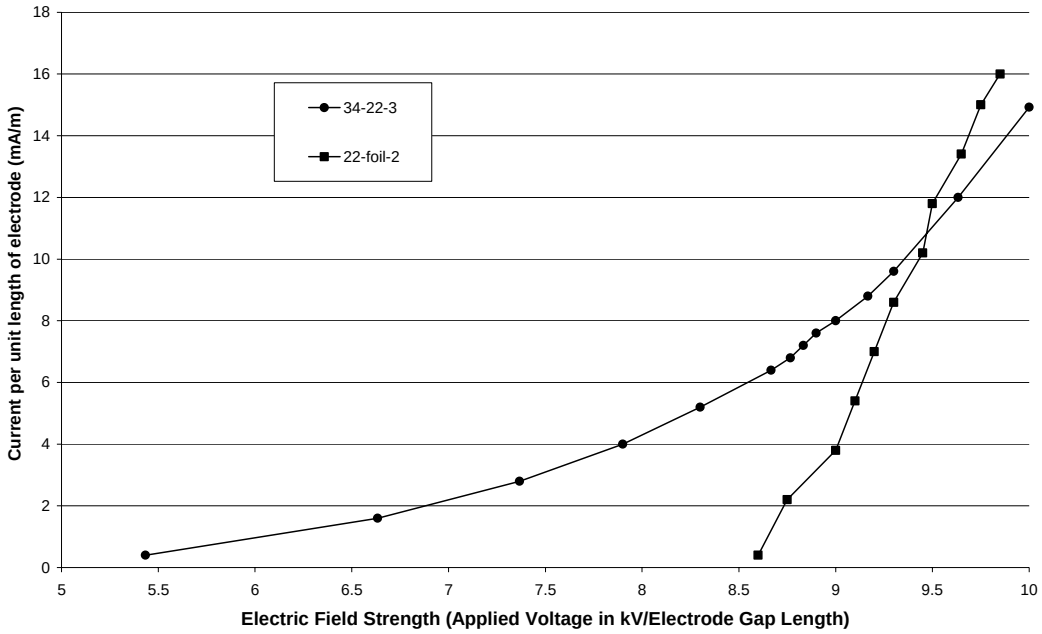

Figure 3.1.9 Current per unit length of electrode versus electric field strength for electrode configurations 34-22-3 and 22-foil-2

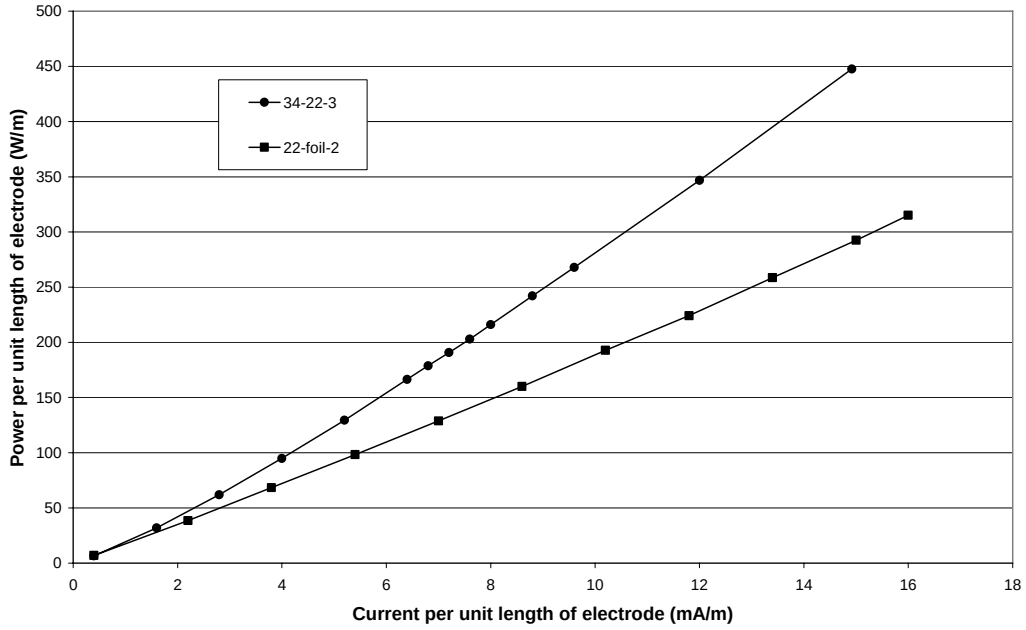

Figure 3.1.10 Power per unit length of electrode versus current per unit length of electrode for electrode configurations 34-22-3 and 22-foil-2

As can be seen from the figures above, the two electrode pairs produce a similar amount of discharge current; however, the 22-foil electrode pair requires much less power to do so. The 34-22 configuration has a wider operating range, greater stability, and a much lower discharge onset voltage. An interesting aspect of testing these two configurations further is the effects of the mixed electrode geometry on the production of the ion-induced force. Both pairs feature electrodes with unequal emission radii that give them greater stability.

3.1.4 Negative-Bias Electrode Tests

As previously discussed, initial tests and literature review led to the desire for a second power supply that would deliver high voltage at a negative potential. El-Khabiry and Colver [14] performed simulations in which the downstream electrode was set to a negative bias. This negative sink provided a preferred path for the positive ions created by the corona discharge upstream. Charge losses to the surroundings were eliminated and, as predicted, larger current values were obtained for a given local electric field strength. When these tests were performed using the -2 kilovolt DC power supply for the two selected electrode configurations, there was an increase in discharge current relative to the experiments in which the downstream electrode was at ground potential.

3.2 Flat Plate Boundary Layer Velocity Profile Measurements

The emitter/receptor pair was mounted flush to the flat plate surface 5 centimeters from the leading edge. Boundary layer velocity profiles were measured 5 centimeters downstream from the electrode pair for four free-stream velocity magnitudes (U = 2.5, 5, 7.5, and 10 m/s) using two electrode configurations as previously described. Each electrode pair was tested at three current discharge values (I = 0.5, 0.75, and 1.0 mA) with the velocity profile measured for each setting. The 1.0 mA current setting was generated using both the positive and negative high voltage power supplies.

3.2.1 Results for Electrode Pair 1: 34-22-3

The 34-22-3 electrode configuration was tested at four free-stream velocity magnitudes and at three current corona discharge values. Figures 3.2.1 through 3.2.4 provide plots of the boundary layer velocity profiles for the four test settings.

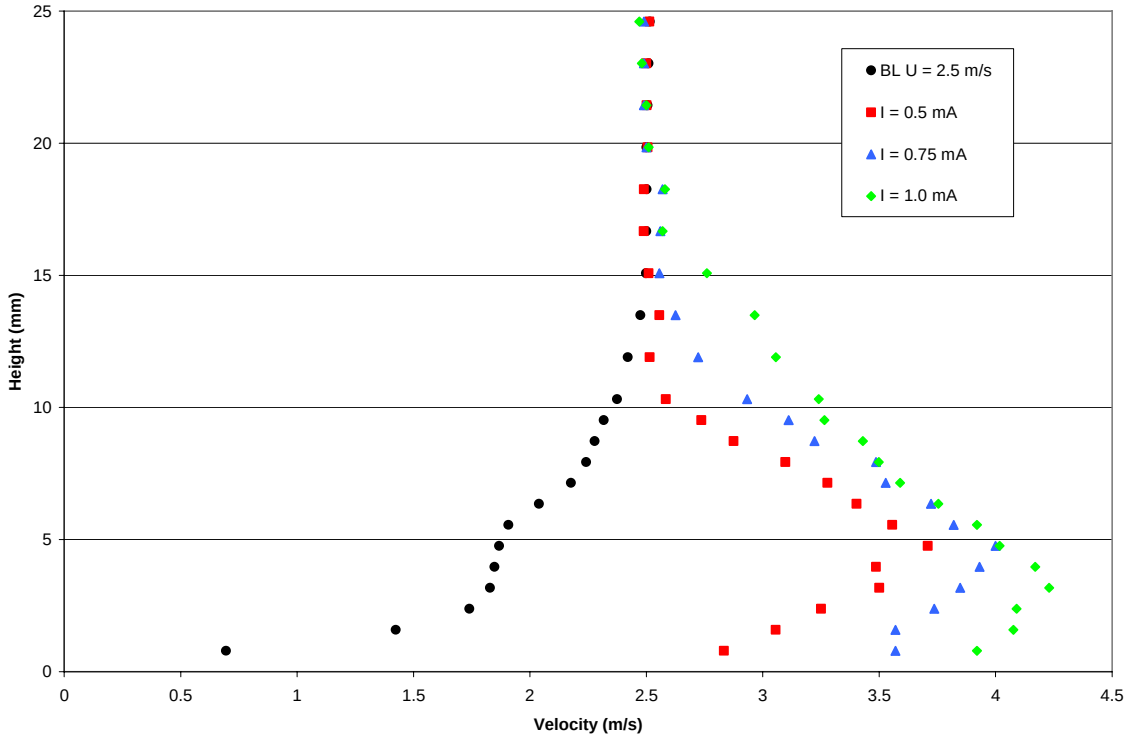

Figure 3.2.1 Boundary layer velocity profiles for no ion flow control (BL) and for three IFC current settings at free-stream velocity U = 2.5 m/s for the 34-22-3 electrode pair

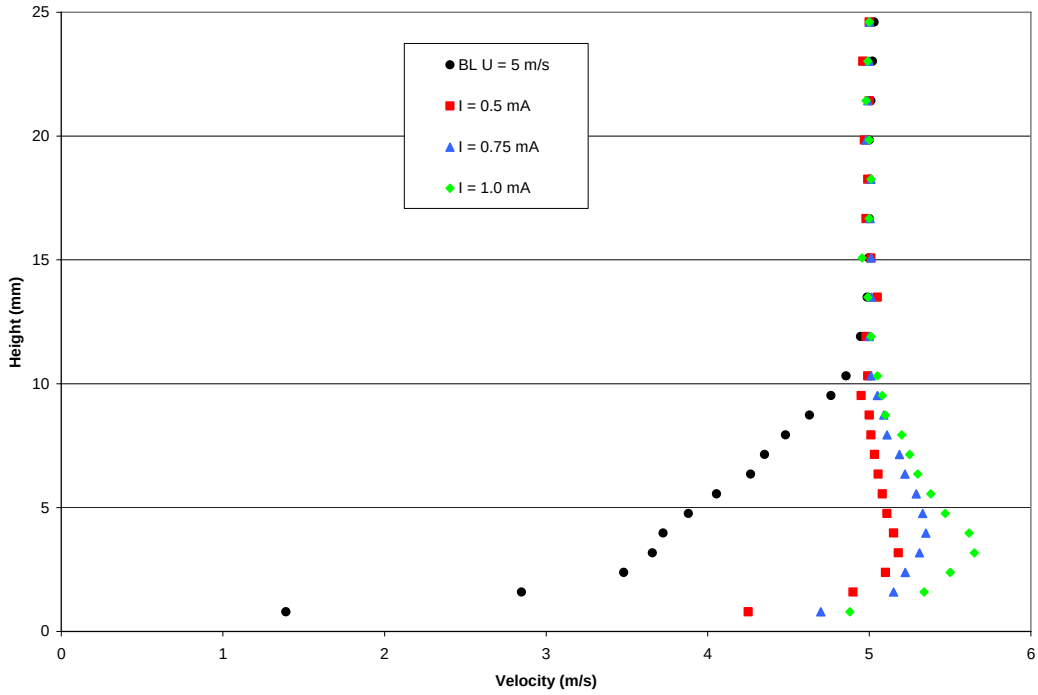

Figure 3.2.2 Boundary layer velocity profiles for no ion flow control (BL) and for three IFC current settings at free-stream velocity U = 5 m/s for the 34-22-3 electrode pair

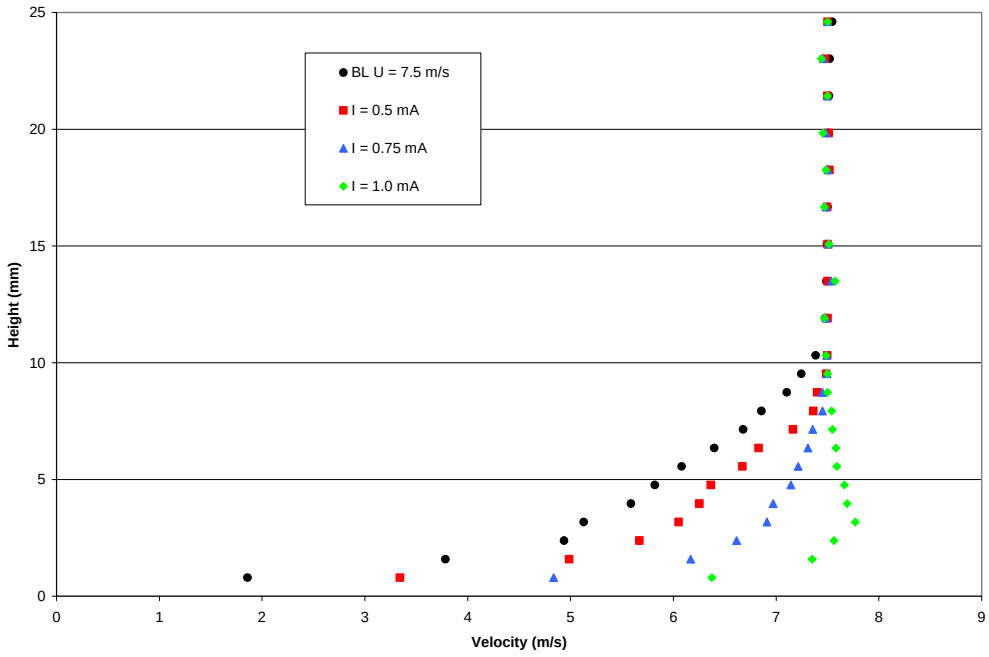

Figure 3.2.3 Boundary layer velocity profiles for no ion flow control (BL) and for three IFC current settings at free-stream velocity U = 7.5 m/s for the 34-22-3 electrode pair

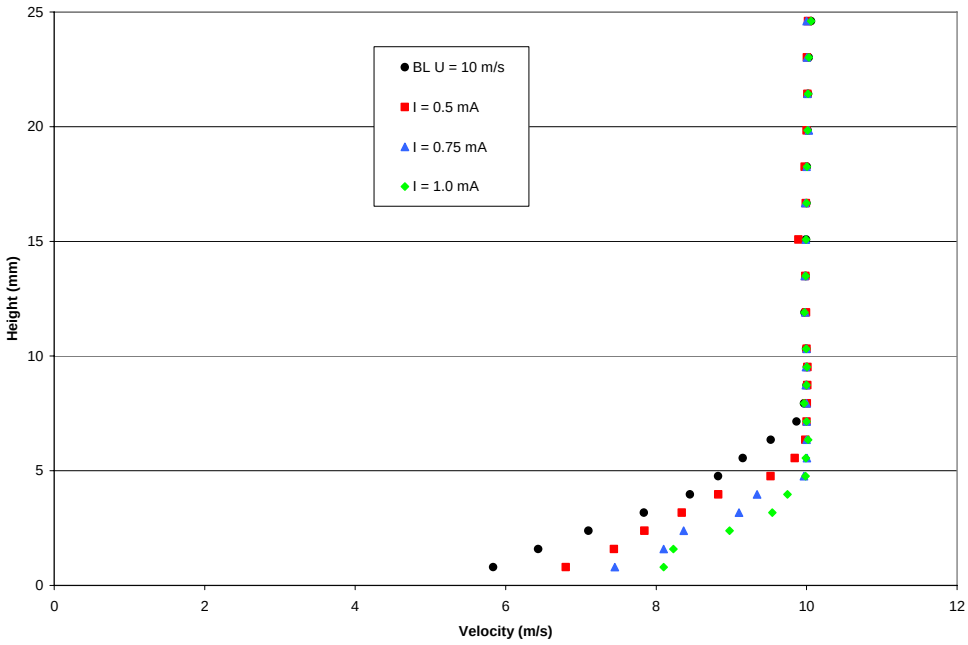

Figure 3.2.4 Boundary layer velocity profiles for no ion flow control (BL) and for three IFC current settings at free-stream velocity U = 10 m/s for the 34-22-3 electrode pair

The ion-induced body force accelerates the flow in the near-wall region increasing the velocity magnitudes within the boundary layer. For a free-stream velocity magnitude of 2.5 m/s, the boundary layer thickness is increased; however, the opposite is true for free-stream magnitudes of 5, 7.5, and 10 m/s. The increase in boundary layer thickness for the lowest free-stream magnitude is likely due to the large increase in momentum due to the ion-induced force. The low energy flow is more highly disturbed by the corona discharge and the effect of the ion flow control penetrates the flow to a greater height. As expected, this effect increases with the discharge current, and the increase in near-wall velocities is greater for lower free-stream velocity magnitudes. For the case of a free-stream velocity of 2.5 m/s, the force is large enough in magnitude to increase the flow velocity to well above the free-stream value. This creates a "bump" in the boundary layer profile. The maximum velocity generated by ion flow control is 4.23 m/s, almost double the free-stream magnitude. The height above the plate surface at which the maximum velocity is reached decreases as the discharge current increases. Once the maximum velocity

magnitude is reached, the velocity slowly decreases and the boundary layer profile begins to take the shape of a typical undisturbed flow field.

As the free-stream velocity magnitude is increased, the boundary layer profile "bump" begins to disappear. While the "bump" appears for all current settings at the 5 m/s free-stream velocity case, it is only noticeable for the 1.0 mA current value at the 7.5 m/s free-stream case. Once the free-stream velocity is increased to 10 m/s there are no longer near-wall velocity magnitudes that are greater than the free-stream magnitude. However, the boundary layer thickness is reduced by approximately 50% for the 1.0 mA current setting when compared to the profile with no ion flow control.

3.2.2 Results for Electrode Pair 2: 22-foil-2

As with the first electrode configuration, the 22-foil-2 electrode configuration was tested at four free-stream velocity magnitudes and at three current corona discharge values. Figures 3.2.5 through 3.2.8 provide plots of the boundary layer velocity profiles for the four test settings.

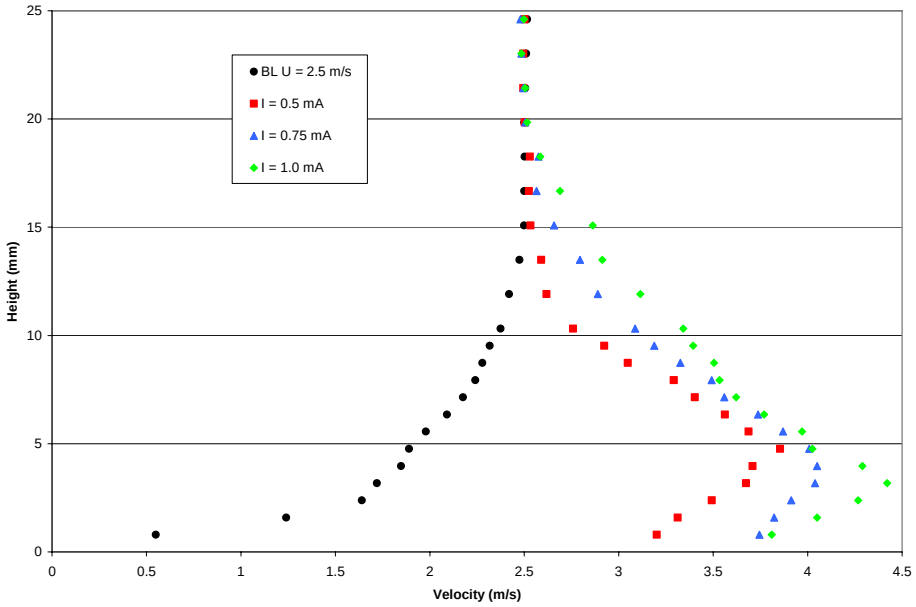

Figure 3.2.5 Boundary layer velocity profiles for no ion flow control (BL) and for three IFC current settings at free-stream velocity U = 2.5 m/s for the 22-foil-2 electrode pair

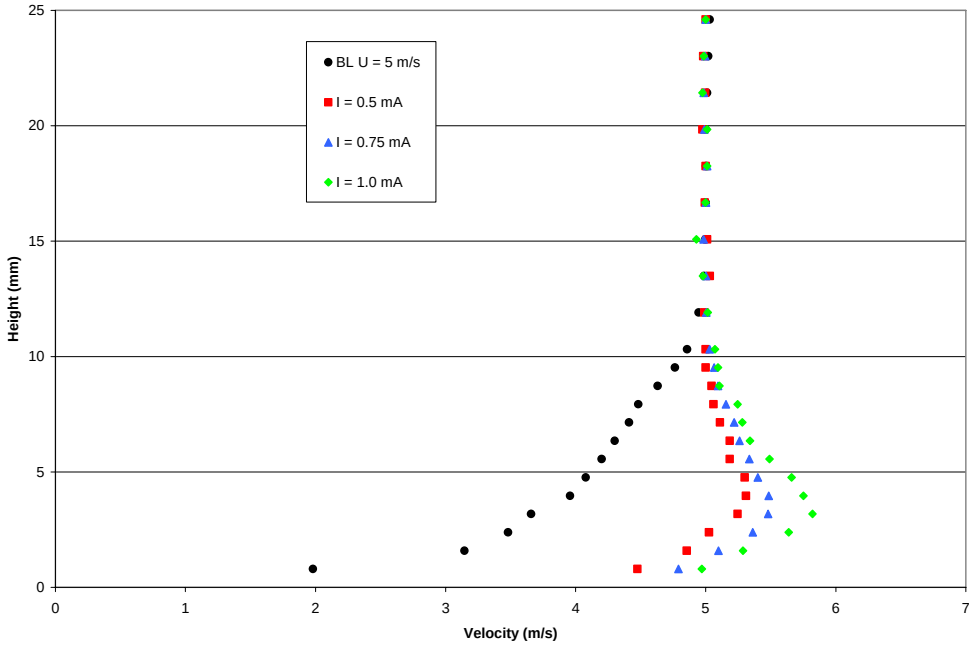

Figure 3.2.6 Boundary layer velocity profiles for no ion flow control (BL) and for three IFC current settings at free-stream velocity U = 5 m/s for 22-foil-2 electrode pair

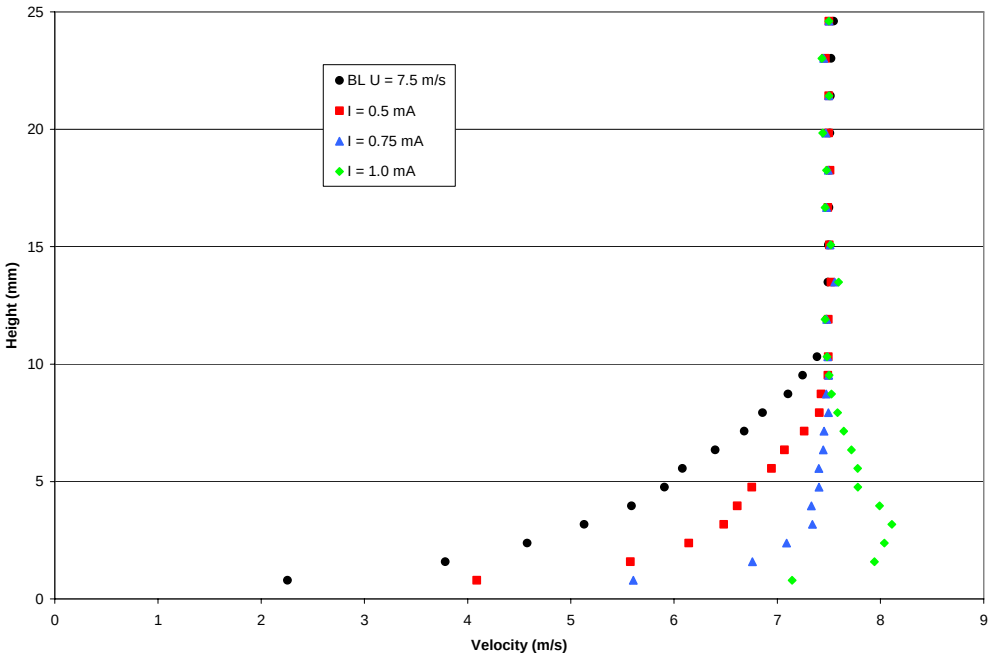

Figure 3.2.7 Boundary layer velocity profiles for no ion flow control (BL) and for three IFC current settings at free-stream velocity U = 7.5 m/s for the 22-foil-2 electrode pair

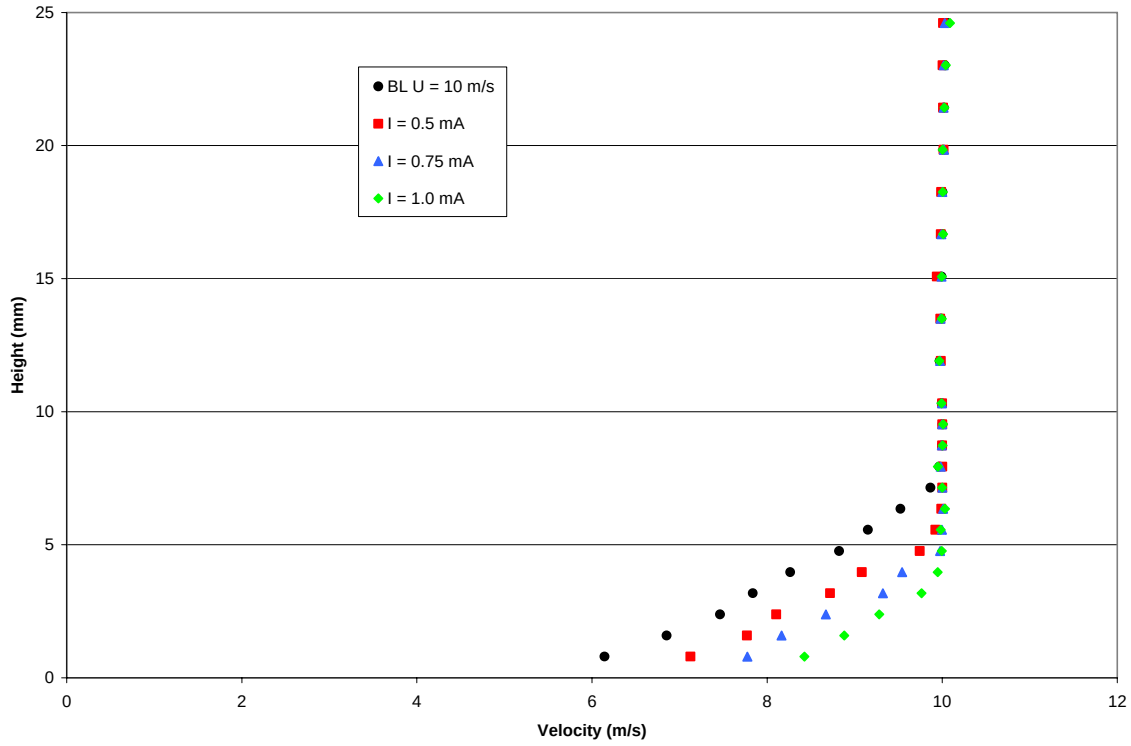

Figure 3.2.8 Boundary layer velocity profiles for no ion flow control (BL) and for three IFC current settings at free-stream velocity U = 10 m/s for the 22-foil-2 electrode pair

The 22-foil-2 electrode flat plate results are similar to those of the first electrode pair. There is a noticeable "bump" in the boundary layer profile that lessens as the free-stream velocity is increased. For the case of a free-stream velocity equal to 2.5 m/s, the ion flow control accelerates the flow to a value of 4.5 m/s. The boundary layer thickness follows the same trends as for the first electrode pair, with an increase for a free-stream velocity magnitude of 2.5 m/s and a reduction for cases with larger free-stream magnitudes. There is a boundary layer thickness reduction of approximately 50% for the 10 m/s free-stream case. Specific comparisons of the results of the two electrode configurations are given in the following section.

3.2.3 Comparison of Electrode Configurations

When comparing the two electrode configurations, the near-wall velocity magnitudes are seen to be greater for the 22-foil-2 configuration for all free-stream velocity magnitudes tested. This was expected, however, since the electric field required to generate the same current value was larger for the 22-foil-2 pair. The shorter electrode gap length led to a greater localized field strength that imparted a larger electrostatic force on the positive ions in the flow. That is not to say that the 22-foil-2 configuration is necessarily a better electrode arrangement. The ion-induced body force seems to be wholly determined by the discharge current and the electric field required to generate that current value. The best configuration is one that most efficiently ionizes the incoming air and drives the positive ions to the downstream electrode. Therefore, an ideal electrode configuration would involve an upstream, positive electrode with a small radius of curvature to ensure the greatest field emission. The downstream electrode would need to act as a sink for the positive ions, thus a negative-biased receptor is the ideal choice. To provide stability the two electrodes would need to have unequal radii to widen the operating envelope for the positive corona discharge.

An interesting observation is that the electrode geometry did not affect the nature of the boundary layer velocity profile. Although the 22-foil-2 configuration produced a greater acceleration of the flow within the boundary layer, the velocity profiles for the two electrode pairs were similar in all test cases. The force produced by the corona discharge seems to act tangentially to the flow and close to the surface. These are promising discoveries for the ability to model ion flow control.

3.2.4 Velocity Measurement Accuracy

As previously stated, an error analysis of the instrumentation used in this study was performed by colleague Michael Perry. From Perry's thesis, the uncertainty of measured velocity magnitudes was ± 0.07 m/s [17]. Error was minimized by recording differential pressure values from the transducers when measuring the velocity. In order to illustrate

the associated error with the velocity measurements, Figure 3.2.9 shows the boundary layer velocity profiles for no ion flow control and for three discharge current settings at a free-stream velocity of 2.5 m/s for the 34-22-3 electrode pair with error bars.

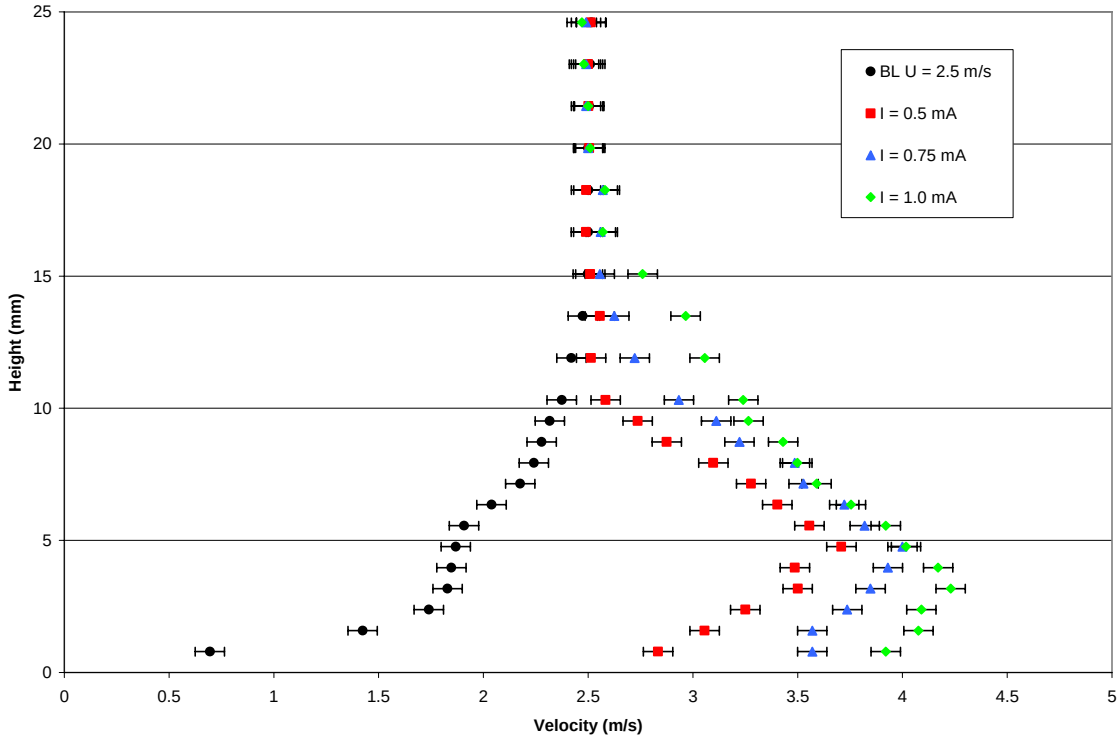

Figure 3.2.9 Boundary layer velocity profiles for no ion flow control (BL) and for three IFC current settings at free-stream velocity U = 2.5 m/s for the 34-22-3 electrode pair with error bars to show uncertainty of velocity measurements

3.3 Cascade Static Tap Measurements

Following the testing methodology of Perry [17], static tap data was used to characterize separated flow over blades in the low-speed compressor cascade. In Perry's parametric study on the effects of free-stream turbulence on separated flow, the static tap data was paired with surface oil flow visualizations to determine separated flow behavior for a wide range of Reynolds numbers in the cascade. Perry observed trailing edge separation for a stagger angle $\xi = 25^{\circ}$ and an angle of attack $\alpha^* = 6^{\circ}$ for all Reynolds numbers tested. For a stagger angle of 25° and $\alpha^* = 12^{\circ}$, the cascade demonstrated both leading and

trailing edge flow separation. Four test cases were selected to examine the effects of ion flow control in the cascade.

3.3.1 Separated Flow Cases

Before instrumenting the blades with electrodes, cascade test setups needed to be found that exhibited separated flow at the low speeds being examined in this study. As discussed above, the cascade arrangements of a stagger angle of 25° and angles of attack of 6° and 12° were tested. At Reynolds numbers of 60k, 90k, and 125k, based on blade chord, Perry observed separated flow. For the free-stream velocity magnitudes used in the flat plate experiments, the corresponding Reynolds numbers, based on blade chord length, were 10k for 2.5 m/s, 20k for 5 m/s, 30k for 7.5 m/s, and 40k for a free-stream velocity of 10 m/s. Tests were run for the 5 m/s and 10 m/s velocity magnitudes and the static pressure was measured at each static tap location along the blade chord. Performance was characterized by the static pressure coefficient, $C_{ps,blade}$, defined below.

$$C_{ps,blade} = \frac{P_{s_1} - P_{s_b}}{P_{t_1} - P_{s_1}} \tag{1}$$

where P_{s1} is the static pressure measured in the calibration section of the wind tunnel upstream of the cascade; P_{sb} is the static pressure measured with taps on the blade surface; and P_{t1} is the total pressure measured in the calibration section at the same location as P_{s1}. Figure 3.3.1 is a plot of blade suction side static pressure coefficient at each chord station along the blade for the case of $\xi = 25º$, $\alpha^* = 6°$, and U = 5 m/s.

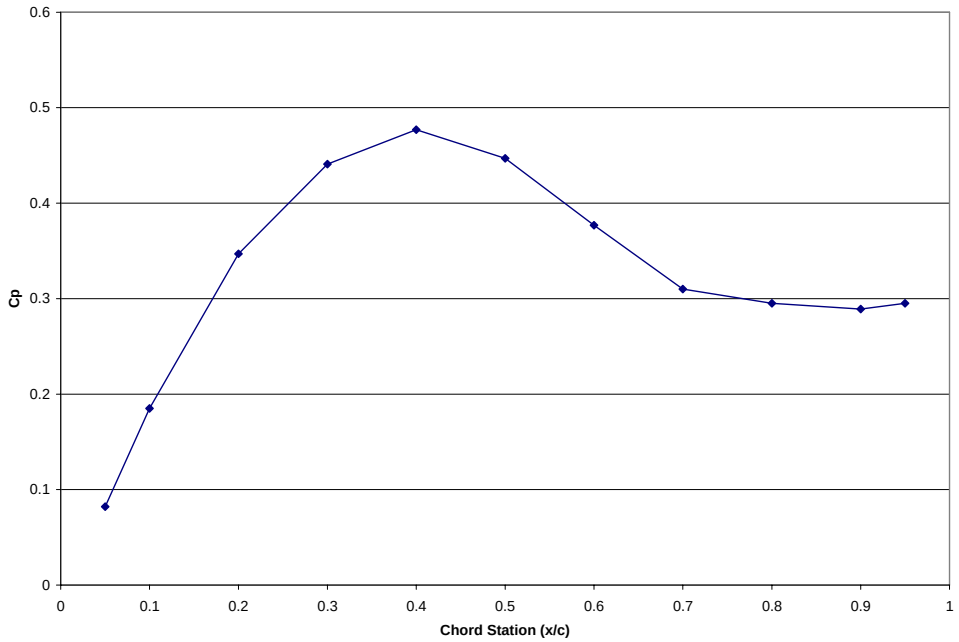

Figure 3.3.1 Suction side static tap data for $\xi = 25º$, $\alpha^* = 6°$, U = 5 m/s

As expected, this cascade test setup exhibited separated flow along the last 20% of the blade chord. The same experiment was run for a free-stream velocity of 10 m/s. The plot of $C_{ps,blade}$ versus chord station is shown in Figure 3.3.2.

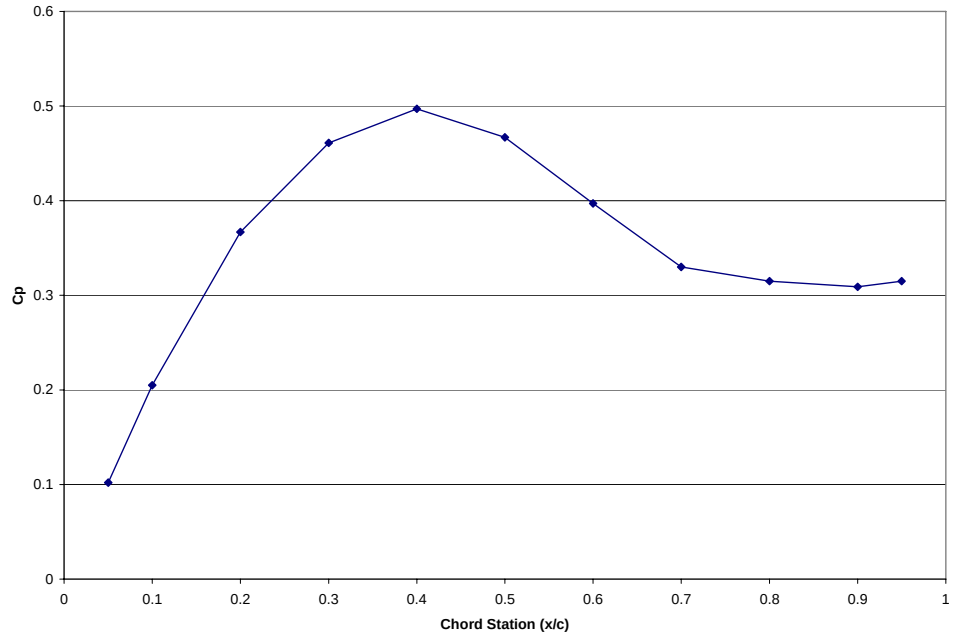

Figure 3.3.2 Suction side static tap data for $\xi = 25º$, $\alpha^* = 6°$, U = 10 m/s

As with the U = 5 m/s case, the static pressure coefficient data showed trailing edge separation for a free-stream velocity magnitude of 10 m/s.

The second cascade setup that was tested was for a stagger angle of 25° and an angle of attack of 12°. Static tap measurements were taken for free-stream velocities of 5 and 10 m/s. The results are plotted below in Figures 3.3.3 and 3.3.4.

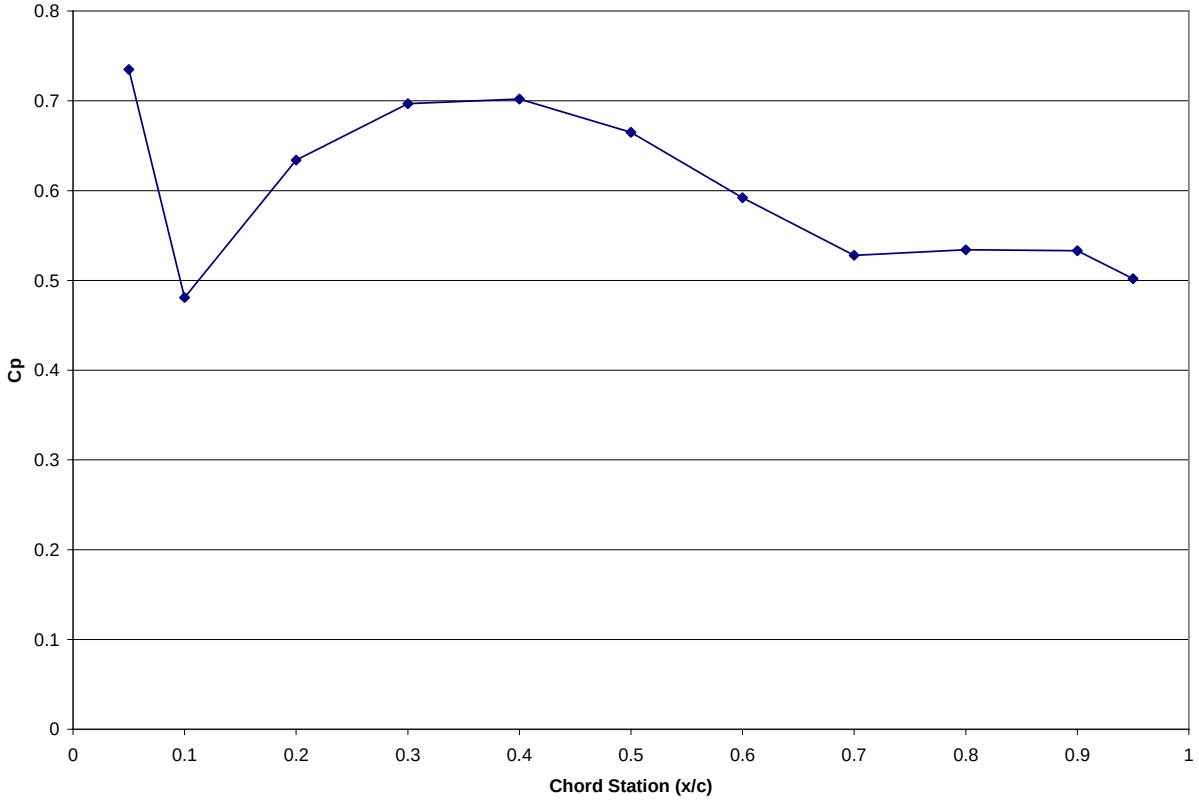

Figure 3.3.3 Suction side static tap data for $\xi = 25^{o}$, $\alpha^{*} = 12°$, U = 5 m/s

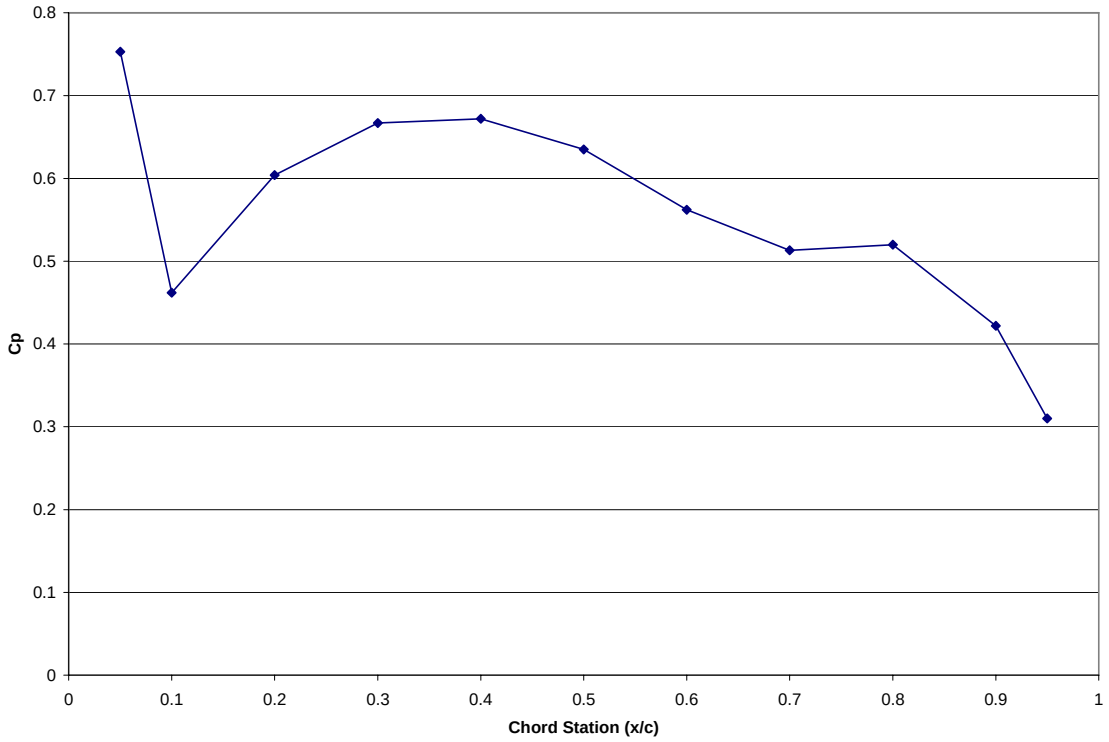

Figure 3.3.4 Suction side static tap data for $\xi = 25º$, $\alpha^* = 12°$, U = 10 m/s

Both of the above cases exhibited leading edge separation; however, there was also trailing edge separation behavior present. For the case of U = 5 m/s, the flow reattaches at approximately 10% chord and then due to frictional losses along the blade surface separates at the 70% chord station. With the free-stream velocity set to 10 m/s, the flow once again reattaches at 10% chord. There appears to be a separation bubble that occurs around 70% chord that disappears at the trailing edge of the blade. With the higher energy of the 10 m/s flow is able to reattach in the aft portion of the blade.

These four cascade flow provide a variety of examples for investigating the effects of ion flow control.

3.3.2 Ion Flow Control Tests on Separated Flow in a Compressor Cascade

In order to incorporate ion flow control in the VT low-speed compressor cascade, an electrode pair was flush mounted to the center blade of the cascade row. The blade

featured static pressure taps along its suction surface, which allowed for the effects of ion flow control on separated flow to be measured. The four cases tested above where used to investigate the ability of a corona discharge to reattach separated flow in the cascade.

For the cases with a stagger angle of 25° and angle of attack of 6°, the emitter/receptor pair was placed at mid-chord. This was done in an attempt to prevent the trailing edge separation exhibited by that cascade setup. The 34-22-3 electrode configuration was used because the thin diameter wires were easier to mount to the blade surface without interfering with the static taps. A sheet of Kapton® dielectric material (100 CR type, 25 μm thick) produced by DuPont was used to prevent arcing to the surroundings. Also, in order to isolate the electrode pair from the cascade test section, the mixed polarity electrode arrangement was used. Figures 3.3.5 and 3.3.6 show the static pressure coefficient data at the two tunnel speeds for no flow control, and for a discharge current of 1.0 mA.

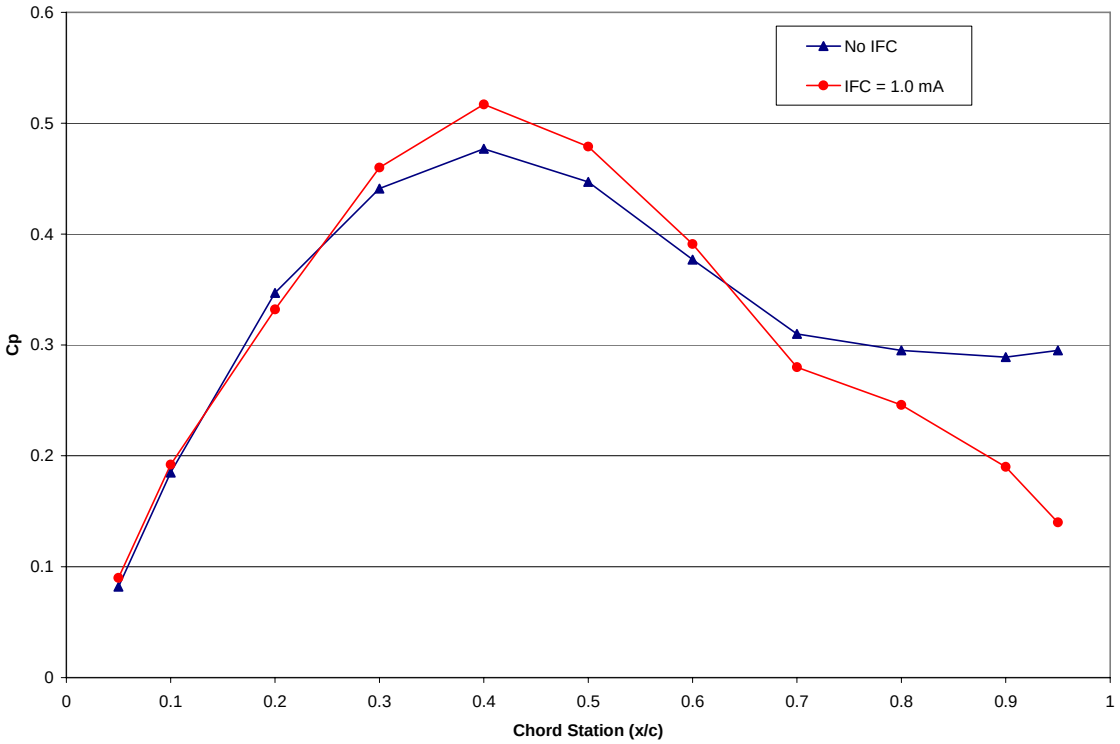

Figure 3.3.5 Suction side static tap data for ξ = 25º, α* = 6°, U = 5 m/s for no flow control (BL) and with IFC current of 1.0 mA

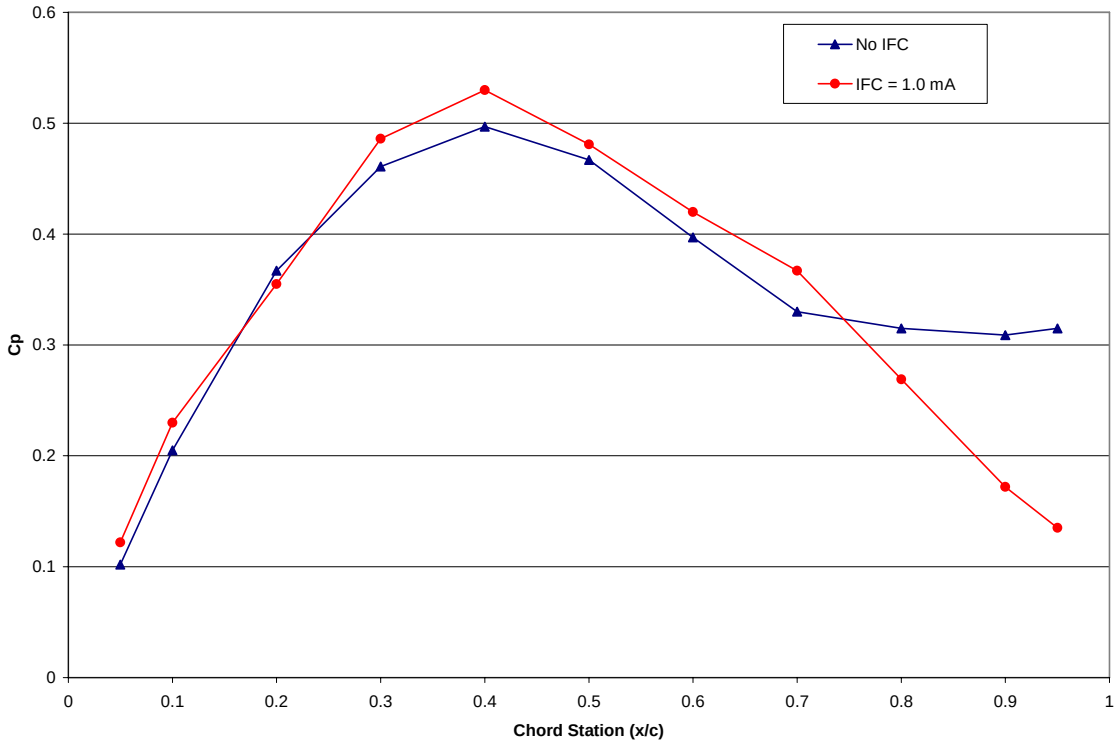

Figure 3.3.6 Suction side static tap data for $\xi = 25^{\circ}$, $\alpha^* = 6°$, U = 10 m/s for no flow control (BL) and with IFC current of 1.0 mA

In both cases, the corona discharge was able to reattach the separated flow over the compressor blade.

For the cascade setup with stagger angle $\xi = 25^{\circ}$ and angle of attack of 12°, the electrode pair was placed at the leading edge of the blade. The pair was arranged as such in order to prevent the separation at the blade's leading edge. As for the case of $\alpha^* = 6°$, the 34-22-3 emitter/receptor configuration was used at a corona discharge current of 1.0 mA. The results of these tests at free-stream velocities of 5 m/s and 10 m/s are shown in Figures 3.3.7 and 3.3.8.

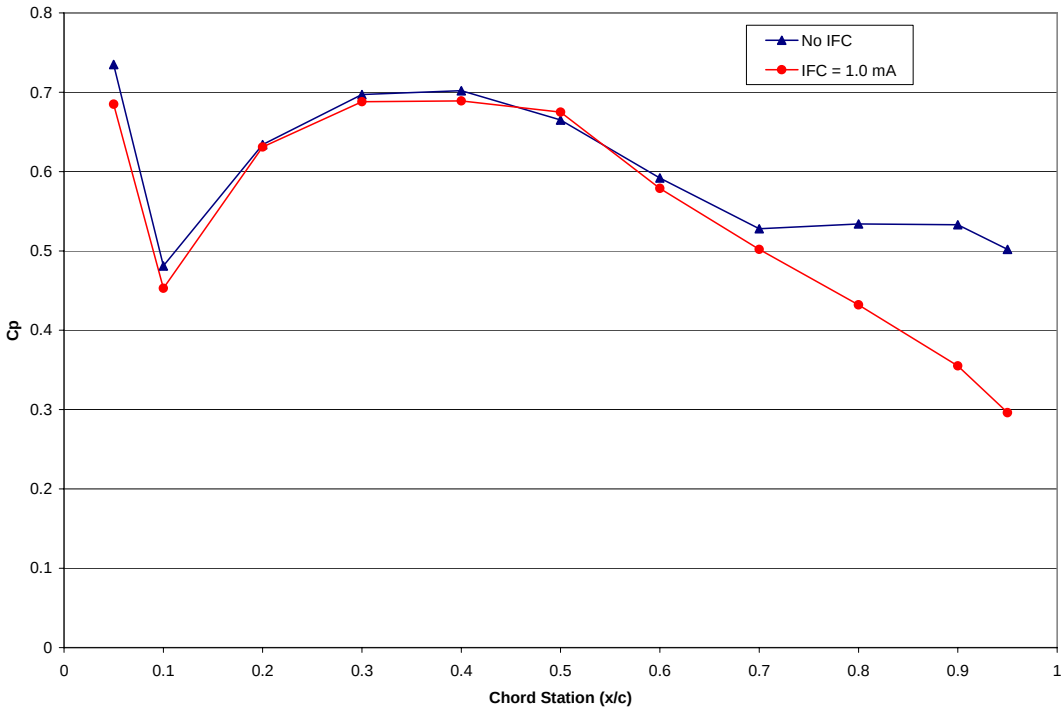

Figure 3.3.7 Suction side static tap data for $\xi = 25^{o}$, $\alpha^{*} = 12°$, U = 5 m/s for no flow control (BL) and with IFC current of 1.0 mA

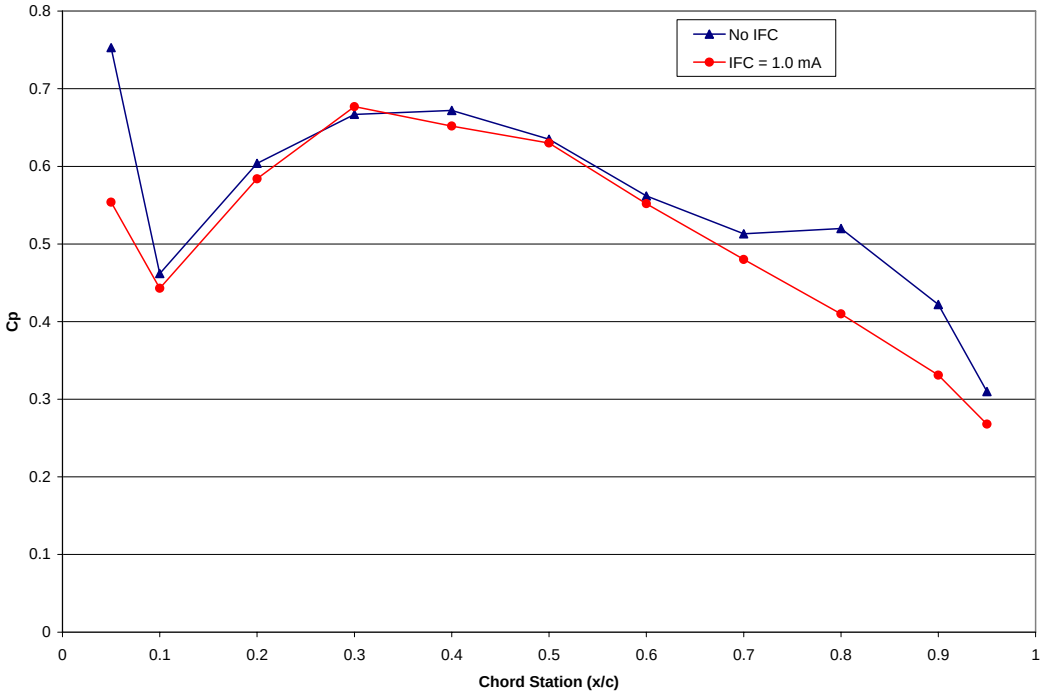

Figure 3.3.8 Suction side static tap data for $\xi = 25^{o}$, $\alpha^{*} = 12°$, U = 10 m/s for no flow control (BL) and with IFC current of 1.0 mA

For the case of U = 5 m/s, ion flow control was unable to prevent leading edge separation. The corona discharge had little effect on the value of the static pressure coefficient at the 5% chord station. The electrode pair did, however, prevent the trailing edge separation that occurred at 70% chord in the no flow control case.

There was a pronounced effect on $C_{ps,blade}$ at the leading edge for the case of U = 10 m/s, but the flow does not appear to be attached. As with the case of free-stream velocity of 5 m/s, the trailing edge separation behavior has disappeared. The separation bubble that was present in the no flow control case is now removed in the ion flow controlled test.

In summary, DC corona discharges showed the ability to affect separated flow behavior in a low-speed compressor cascade. The force generated by a 1.0 mA discharge current was able to prevent separated flow at the trailing edge of the compressor cascade for all setups tested. The force was not sufficient, however, to prevent leading edge separation, although some effect on the flow was seen. It is possible that the electrode pair was not properly oriented to correct the leading edge separation for the 5 and 10 m/s free-stream velocity cases. The pair was placed as close to the leading edge as physically possible; however, it seems that the electrode pair is placed after the separation point. In order to prevent separated behavior, the ion-induced body force must be applied before the separation point.

Chapter 4

Computational Model

One driving factor of this research was the development of a CFD model that could be used in the design of future experimental work. This chapter contains the details of the resulting computational model including the selection of the numerical solver and turbulence model, grid generation, and ion flow implementation through User-Defined Functions (UDF's). Using theoretical gaseous discharge principles, a generalized UDF was developed to model the ion flow control that could be applied to all experiments conducted in this study. The validation of this model provides a design tool that allows for further investigation of the merits of ion flow control.

4.1 CFD Motivation

The scope of this research was not only to develop a foundation of ion flow control experimental techniques at the VT Turbo Lab, but also to provide a Fluent CFD model of the flow control scheme. A reliable computational model can be used as a prolific design tool. By creating a model based on the principles of gas discharge physics and validated with experimental data, new ideas can be explored based on the capabilities of current electrode designs.

4.2 CFD Model

Fluent® is widely used in both academic and industrial research applications. Its availability to the VT Turbo Lab members makes it a convenient computational software to use. Some features of Fluent made it an obvious choice to create a numerical model for ion flow control. Through the creation of UDFs, the user can make additions to the governing equations. By adding a source term to the momentum equation, the user can simulate the addition of a body force such as the electrostatic force associated with ion flow control.

4.2.1 Computational Model Geometry and Boundary Condition Setup

In order to numerically model the results of this study, a computational domain was developed for each test platform with boundary conditions based on experimental settings. Modeling a flow in Fluent requires setting up boundary conditions at the inlet and outlet as well as specifying any solid surfaces. Fluent allows various methods for prescribing the flow field at the inlet boundary. The method employed for the flat plate was a pressure inlet. For this boundary type, the inlet static and total pressures, along with the direction of the incoming flow, are entered by the user. From these values, the magnitude of the velocity at the inlet is computed by Fluent. Both the inlet and static pressure are measured in the calibration section of the wind tunnel. It is from this location that the inlet flow parameters are measured for the computational case. The flat plate test platform was positioned at the exit of the calibration section during testing. Therefore, the inlet for the flat plate model was defined as the top-half of the calibration section exit plane. A diagram of the computational domain for the flat plate is shown below in Figure 4.2.1.

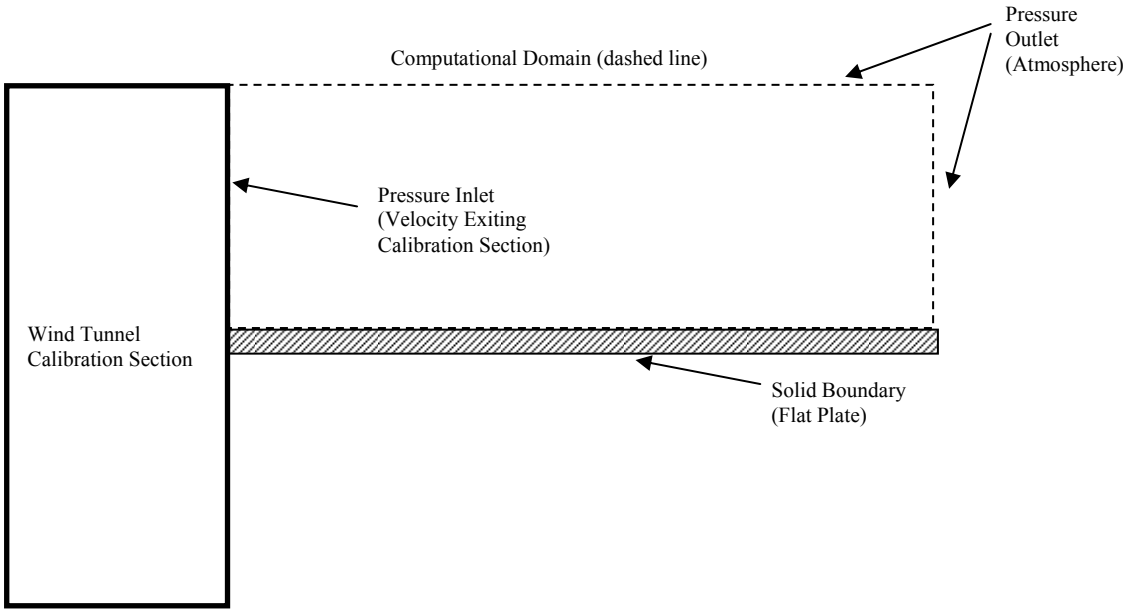

Figure 4.2.1 Computational domain of the flat plate test platform outlining the boundary conditions used for the numerical model

A pressure outlet was used as an exit boundary condition. Because the test platform is exposed to the atmosphere, the pressure at the boundary above the plate at the height of the calibration section and the end of the flat plate were set to zero for gauge pressure measurements. The surface of the flat plate was given the wall (solid surface) boundary designation. This ensured the no-slip condition along the flat plate.

To model flow through a cascade, periodic boundary conditions must be utilized. A domain was developed that modeled the flow over one airfoil with boundaries at mid-pitch that allowed flow leaving the domain to reenter at its linked periodic boundary. The computational domain for the cascade test section is shown in Figure 4.2.2 below.

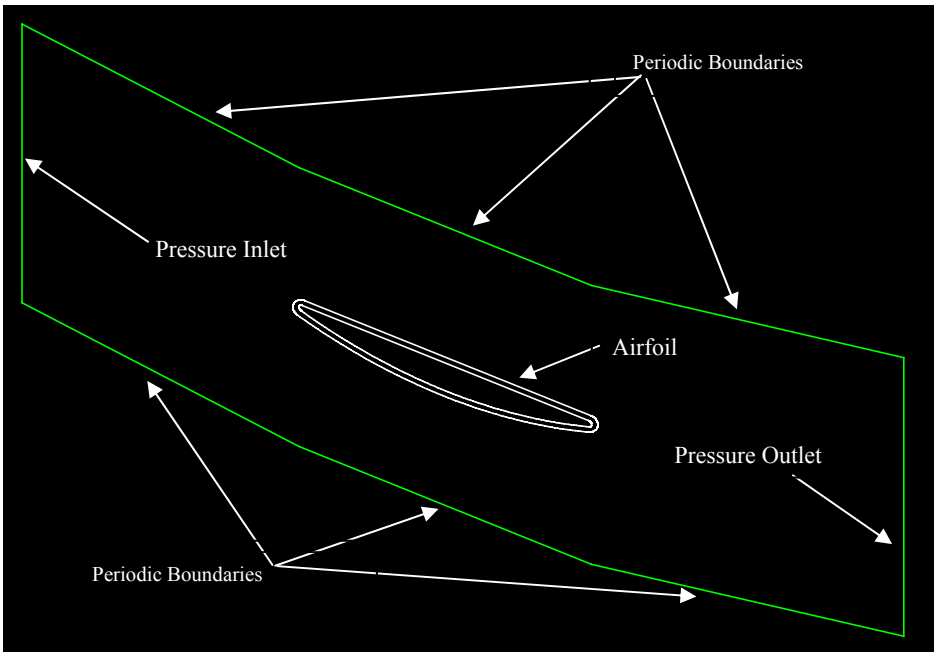

Figure 4.2.2 Computational domain of the cascade outlining the boundary conditions used for the numerical model

The cascade computational model was given a pressure inlet boundary condition. As with the flat plate domain, a pressure outlet boundary was used. Because the cascade discharges to the atmosphere, the pressure at this boundary was also set to atmospheric, or zero for the case of gauge pressures. A wall condition was used for the blade surface.

4.2.2 Turbulence Model Selection

Fluent uses the Navier-Stokes equations to solve aerodynamic flows through the Reynolds Averaged Navier-Stokes (RANS) method. Thus, turbulence effects are averaged and applied to the momentum equation as Reynolds stresses. This is a less-computationally expensive method compared to Direct Numerical Solutions (DNS) or Large-Eddy Simulations (LES), which solve a more complex set of the Navier-Stokes equations. However, accurately modeling turbulence can be difficult using RANS. The methods in which the Reynolds stresses are approximated are determined by the turbulence model applied to the flow. The Walters and Leylek (2003) k-k_L-ω transitional flow model uses three transport equations to approximate the effect of turbulence [18, 19]. Other Fluent models assume turbulent flow at the inlet boundaries, whereas Walters's model uses a prescribed turbulence intensity and allows the flow to transition along the airfoil surface through fluctuations of laminar kinetic energy, k_L, and turbulent kinetic energy, k by means of a specific dissipation rate, ω.

Colleague Darius Sanders has shown that the Walters turbulence model accurately predicts transitional and separated flow in a highly-loaded LPT blade [20]. Sanders's work was conducted for flow that exhibited an adverse pressure gradient past mid-chord; a similar flow condition to that seen in the VT Low-Speed Wind Tunnel. Therefore, the Walters transitional flow model was selected for this numerical investigation.

The turbulence model depends on values of the turbulent kinetic energy, which is responsible for the production of turbulence; the laminar kinetic energy, which defines the turbulence created in the laminar section of the boundary layer; and the specific dissipation, which controls the dissipation of small scale turbulence into viscous losses [18]. Fluent provides four specification methods for the Walters model that include various groupings of parameters such as the laminar KE, the turbulent KE, the specific dissipation rate, the turbulence intensity, and the integral turbulent length scale. Based on the experimental methodology of the wind tunnel, the turbulence intensity and integral turbulent length scale are well characterized for a wide range of free-stream velocity

operating conditions. Therefore, the selected specification method requires the known turbulence intensity and length scale for the given test to be modeled as well as the laminar kinetic energy, which is left at its default value for all cases examined.

4.2.3 User-Defined Functions

A UDF is a function that can be dynamically loaded into Fluent to enhance the standard features of the code. Through the use of UDFs, physical properties of materials, boundary conditions, and source terms may be added to better tailor Fluent's solver to the user's specific case. UDFs are created using the C programming language in a text editor and added to the solution setup through the DEFINE macros provided by Fluent. An important feature of UDFs is that they are entered as specific values that are defined in SI units. This must be taken into consideration when developing functions that specify changes to the solver.

4.3 Grid Generation

The Fluent-paired mesh generating software, Gambit, was used to create the computational domain. It was important to maintain a fine resolution in the boundary layer region of the external flow in order to resolve the turbulent and transitional characteristics. A method that is often used for determining the required mesh density in the boundary layer is to calculate the y+ value for the flow. Y+ is a non-dimensional wall distance that is defined as

$$y^+ = \frac{u_\tau y}{\nu} \tag{2}$$

where y is the distance to the first node, ν is the kinematic viscosity of the fluid, and u_τ is the friction velocity. The friction velocity can be calculated with equation 3

$$u_\tau = \sqrt{\frac{\tau_w}{\rho}} \tag{3}$$

where τ_w is the wall shear stress and ρ is the density of the fluid. The wall shear stress can be approximated using an order of magnitude analysis for the given flow conditions.

Based on papers published by Walters et al. [18, 19] in 2004 and 2005, a y+ value less than unity is desirable for the Walters k-k_L-ω turbulence model. Therefore, it is necessary to choose a first grid point spacing that maintains a y+ value less than 1.

Using Gambit's built-in boundary layer meshing feature, a structured mesh was generated in the near wall region for both the flat plate and cascade models. The boundary layer command allows the user to set the first nodal spacing, or y value from the y+ equation, near the surface boundary. For the experimental flow parameters, this value was determined using a flat-plate boundary layer order of magnitude analysis. This analysis yielded the theoretical boundary layer thickness. The user provides set values for the number of cell rows and the growth rate of those cells in the boundary layer. The desired number of node points within the boundary layer was approximately 10, and a growth factor was set that provided adequate resolution in the theoretical boundary layer. Structured, quadrilateral cells are used to generate the boundary layer mesh.

Such fine resolution is not necessary for the remainder of the computational domain. Also, the flat plate and cascade models required different types of cells in the bulk flow region. The development of each of these grids is discussed in detail below.

4.3.1 Flat Plate Grid Development

The geometry of the flat plate computational domain was shown in Figure 4.2.1 above. As discussed in the previous section, a boundary layer mesh was applied to the near-wall region. The simple rectangular geometry allowed for structured, quadrilateral cells to be applied to the entire flow field. The total number of cells in the grid is 49,740.

4.3.2 Cascade Grid Development

As with the flat plate grid, a boundary layer mesh was used for the cascade computational domain. The structured boundary layer cells were applied along the airfoil surface. The remainder of the mesh is generated using unstructured, triangular pave cells. The combination of structured and unstructured cells renders the cascade grid a hybrid mesh.

A close-up view of the boundary layer mesh and the mixture of structured and unstructured cells is shown in Figure 4.3.1.

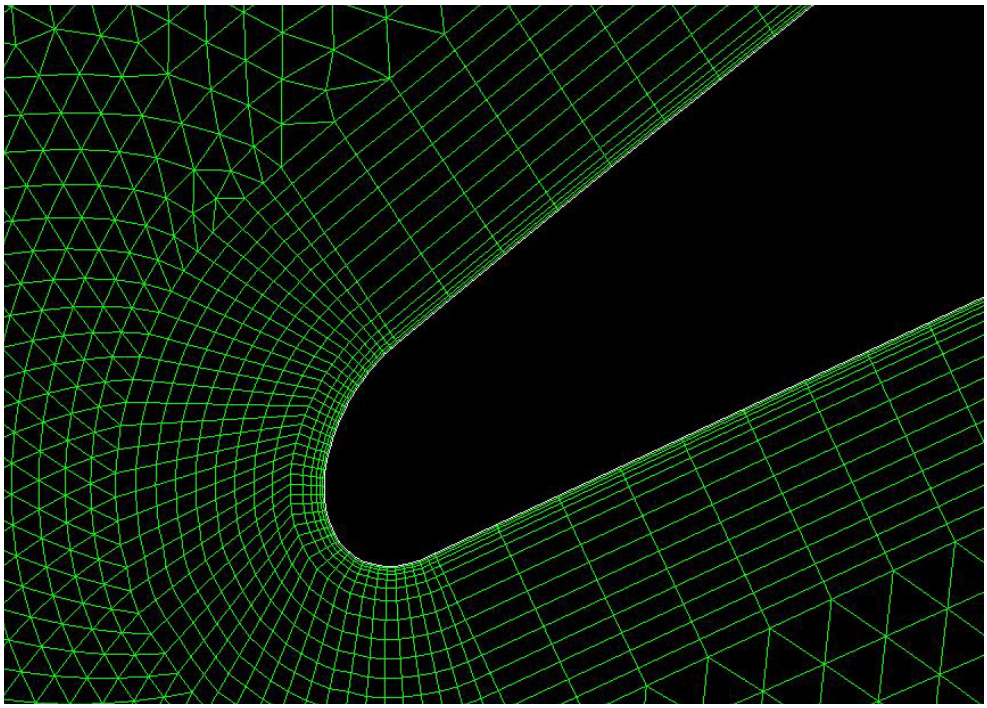

Figure 4.3.1 Zoomed view of the hybrid mesh used for the cascade computational domain

Using a hybrid mesh decreases the grid density and, therefore, shortens computational time. The grid spacing was skewed so that nodes would be concentrated near the wake region, but reduced further away from the blade toward the inlet where the flow field is more uniform. Figure 4.3.2 provides a full view of the cascade grid.

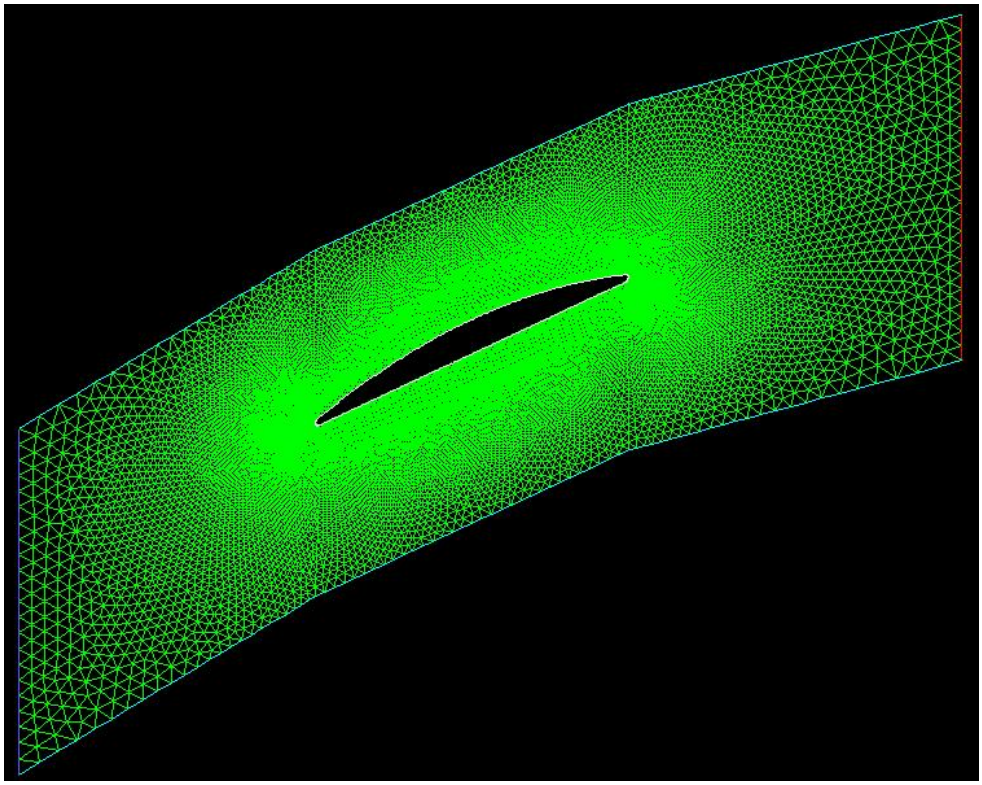

Figure 4.3.2 Full view of hybrid cascade mesh

4.4 Fluent Solver Selection

All calculations were performed in two-dimensions with double precision accuracy. A pressure-based solver was used along with implicit formulation of the discretized functions. A Green-Gause Node Based gradient option was used to ensure accuracy with the hybrid mesh of the cascade model. The viscous (turbulent) solver used was the Walters k-k_L-ω model described above with all default values in the viscous model menu. Derivative formulation was second order for pressure and second order upwind for the momentum and energy equations. Also, the three transport equations required for the turbulence model were second order upwind approximations. The simulation utilizes a coupled pressure-velocity solver for which explicit relaxation factors were set for both momentum and pressure. The Courant number for the coupled solver is set to 25. For this steady-state simulation, the selected Courant number decreases time to convergence. All of the under-relaxation factors, except for the energy equation, were initially decreased to a value of 0.2 to ensure a stable solution. The default value of 1.0 is used

for the energy equation. The under-relaxation factors were increased as the solution developed and the residuals began to decrease. Convergence criteria were increased from the default setting to improve the accuracy of the solution. These criteria were utilized for all simulations and are listed in the following table.

Table 4.4.1 Convergence criteria used for all simulations

Residual	Absolute Criteria
Continuity	1E-05
X-Velocity	1E-05
Y-Velocity	1E-05
Energy	1E-06
K_L	1E-04
K_T	1E-04
ω	1E-04

4.5 Ion Flow Control Modeling

Researchers that have developed complex numerical models for the ion flow control phenomenon have coupled the electrostatic equations of Poisson and charge conservation with the boundary layer equations of continuity and momentum [14]. These models require the computation of electric field strength and ion production, thus limiting the complexity of fluid flows that may be simulated. A more simplified approach, developed to allow for the simulation of complex flow fields, treats the ion-induced force as a source term in the momentum equation [16]. These plasma models rely on experimental parameters to approximate the force and include the source term with the equations of fluid motion. The ion flow control model developed for this research effort incorporates aspects of both of these simulation methods. Using fundamental gas discharge physics and principles of gaseous conductors, the magnitude of the electrostatic force was calculated and implemented in the commercial CFD software through user-defined functions.

4.5.1 Corona Discharge-Fluid Coupling

The ion-induced force was simulated through the addition of a source term to the momentum equation. The body force is used to simulate the collision interaction of positive ions produced by the corona discharge with neutral air molecules not ionized by the electric field. This can be approximated as the force that a local electric field exerts on a charged particle. The equation is given below.

$$F_p = \rho_c E \tag{4}$$

where F_p is the plasma-induced body force per unit volume (N/m^3); ρ_c is the local ion charge density (C/m^3); and E is the local electric field strength (V/m). For this approximation, the effect of negative ions is ignored based on positive corona discharge theory provided by Cobine [3].

In order to determine the charge density of the plasma-affected region, the equation for current density found in El-Khabiry and Colver [14] was used. This equation includes the conduction and convection terms for calculating current density.

$$J = \rho_c (KE + U) \tag{5}$$

where J is the current density (A/m^2); K is the positive ion mobility (taken as 2.2 X 10^{-4} $m^2/V\text{-}s$) [14]; and U is the free-stream velocity (m/s). Plasma characteristic tests provided a full characterization of the DC positive corona discharge for the electrode configurations used in this study. Therefore, the amount of current generated by a given electric field was known. Inserting measured values from plasma characteristic experiments, the amount of force generated by each electrode configuration was calculated. This value was then substituted into a user-defined function to model ion flow control.

4.5.2 Generalized UDF Development

The ion-induced body force was applied to the plasma affected region of the flow field through the development of a generalized user-defined function. Flat plate experimental results showed that the ion flow control had a greater effect near the surface where the electric field was strongest. Therefore, a function was written that applied the plasma force over a specified height with decreasing magnitude away from the plate surface. Also, the force was applied tangent to the surface to which the electrode pair was mounted. Through computational simulations, the plasma affected region was defined as the area with length equal to the electrode gap and a height of one centimeter above the flat plate. The force was then applied to this region with a linearly decreasing magnitude with respect to height. The linear field decay was a tested approximation and the only empiricism used in this fundamental computation model. Figure 4.5.1 below depicts the plasma affected region.

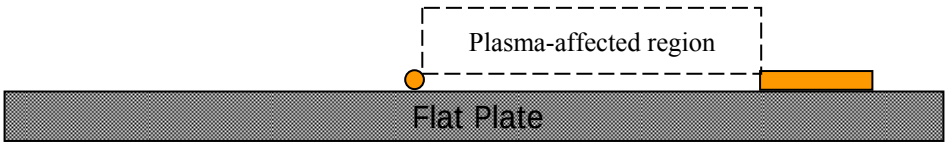

Figure 4.5.1 Plasma-affected region in which ion-induced body force was applied

The UDF was written in the C programming language and added to the solution setup through the DEFINE macros. Once the UDF had been interpreted by Fluent, the fluid boundary condition was changed to accommodate the source term. For flat plate ion flow control modeling, the source was added to the x-momentum equation. In order to apply the force tangential to the airfoil surface during cascade modeling, the force was deconstructed into the x and y vector magnitudes. The force was applied within the computational domain based on the specification of the UDF. Equation 4 above returns the value of the ion-induced body force in SI units of Newtons per cubic meter. In order to illustrate the form of a UDF, the text from a sample function is given below:

```
/* UDF for adding momentum to a fluid */

#include "udf.h"

DEFINE_SOURCE(f_p, c, t, dS, eqn)

{
      real x[ND_ND];
      real source;
      FILE *fp;

      C_CENTROID(x,c,t);
        if (x[0] >= 0.0332 && x[0] <= 0.03485 && x[1] >= -0.0067 &&
x[1] <= -0.0059)

        source = 10000;

      else

      source = dS[eqn] = 0.;

            /*fp = fopen("C:\source.txt", "a");*/

            /*fprintf(fp, "%10f\t%10f\n", x[1], source);*/

            /*fclose(fp);*/

      return source;

}
```

This sample function applies a constant force with a magnitude of 10,000 Newtons per cubic meter within the defined area. Similar files were created in a text editor to simulate the ion-induced force.

Chapter 5

Results of CFD and Comparison with Experiment; CFD Validation

Computational results were obtained for both the flat plate and compressor cascade tests using the ion flow control model discussed in the previous chapter. As detailed above, the ion-induced force was modeled through the use of user-defined functions. Using equations derived from electrostatics and gas discharge physics, the magnitude of the force was calculated and applied tangent to the surface on which the electrode pairs were mounted. Selected numerical results are presented below; first for the flat plate boundary layer profile measurements and then for the cascade static tap data. Plots comparing the numerical data to measured results for every experimental test conducted in this study can be found in Appendix B.

5.1 Numerical Results for Flat Plate Tests

Numerical calculations were performed for each flat plate experiment that was conducted. Overall, the computational simulations showed good agreement with experimental results; however, there were some shortcomings of the CFD model. For the lowest magnitude of free-stream velocity (U = 2.5 m/s), there was an over-prediction of the ion-induced velocities in the near-wall region. The computational model was able to predict the height above the plate surface at which the maximum velocity was reached. The velocity magnitude predicted by the model; however, was off by 0.2 to 0.3 m/s. The model also over-predicted the size of the boundary layer "bump." The numerical results show a greater height above the plate surface at which the plasma-affected velocity magnitude returned to the free-stream value. A comparison of the computational predictions and the experimental results for a free-stream velocity of 2.5 m/s for the 34-22-3 electrode is shown in Figure 5.1.1.

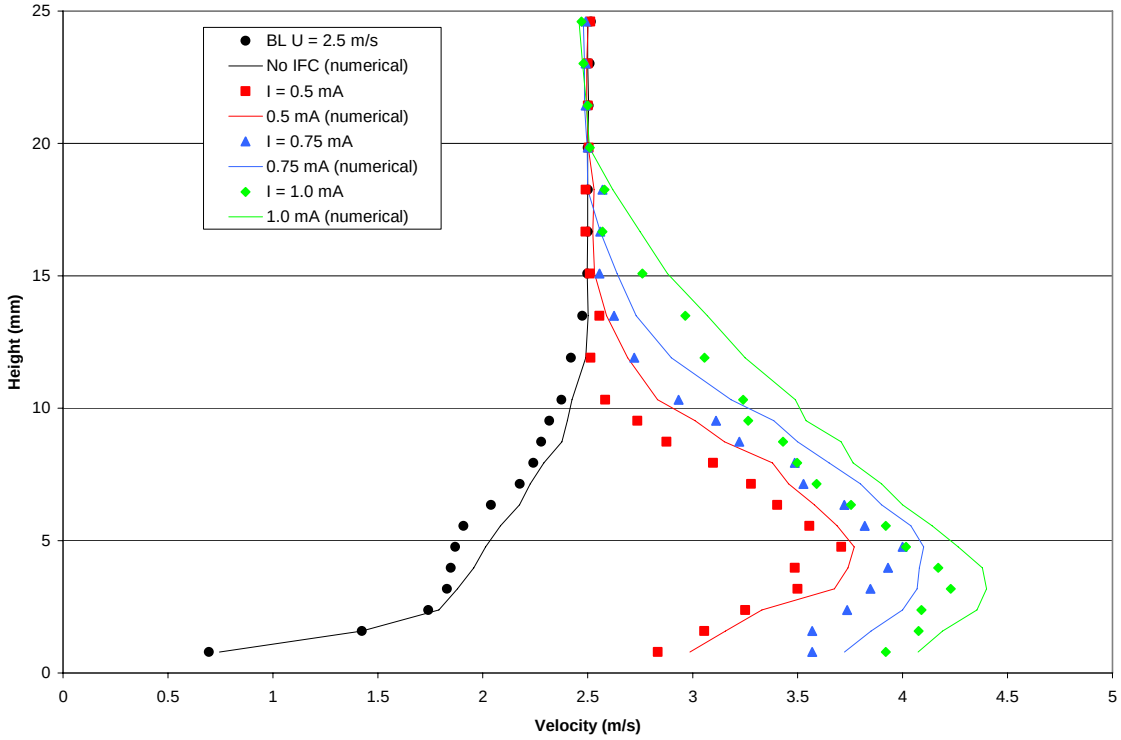

Figure 5.1.1 Numerical and experimental comparison for boundary layer velocity profiles at free-stream velocity U = 2.5 m/s for the 34-22-3 electrode pair

Experiments for the flat plate test case of U = 2.5 m/s were the most difficult to perform due to the outside influence of the atmospheric conditions of the testing facility on the low free-stream velocity. A cause for the increase in numerical inaccuracy for lower free-stream velocity magnitudes could be due to the error associated with the measured velocity values. Figure 5.1.2 shows the same comparison as Figure 5.1.1 but with the error bars in place for the measured velocities.

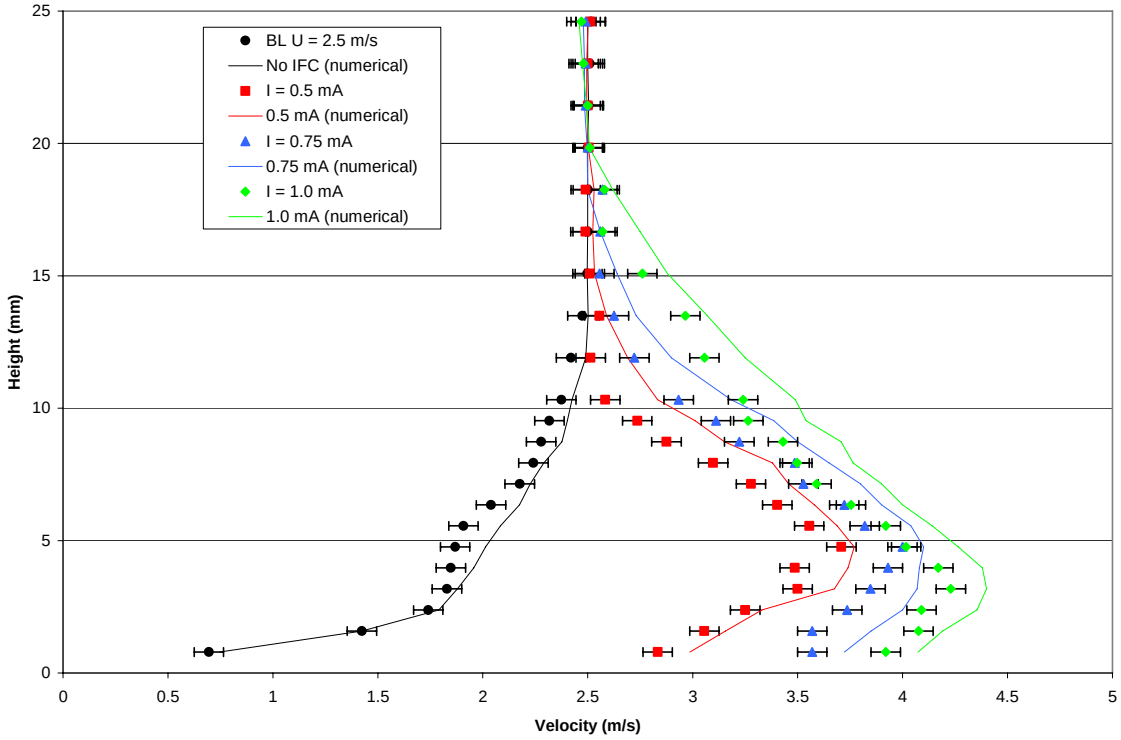

Figure 5.1.2 Numerical and experimental comparison for boundary layer velocity profiles at free-stream velocity U = 2.5 m/s for the 34-22-3 electrode pair with error bars to show uncertainty of velocity measurements

As the free-stream velocity was increased, the model was able to more accurately calculate the velocity magnitudes within the boundary layer. The model was most accurate for the case of U = 10 m/s. At this free-stream velocity, the model very accurately predicted the velocity magnitudes as well as the boundary layer thickness. Figure 5.1.3 shows the numerical and experimental results for the U = 10 m/s case for the 22-foil-2 emitter/receptor design.

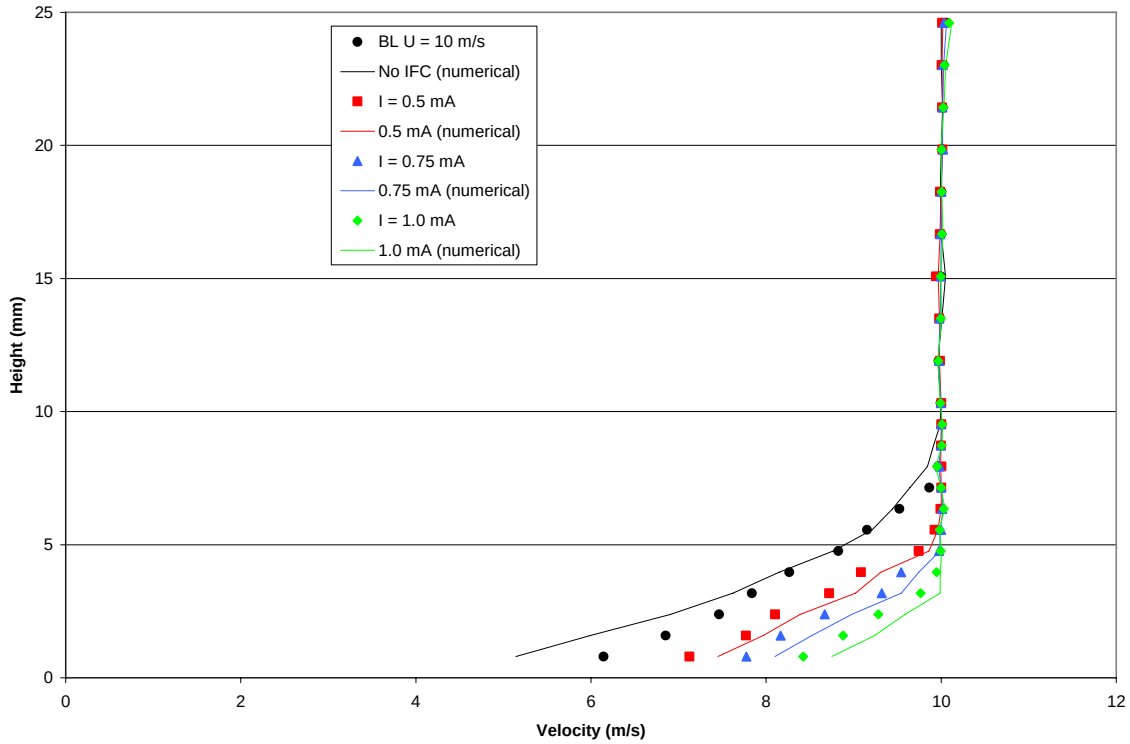

Figure 5.1.3 Numerical and experimental comparison for boundary layer velocity profiles at free-stream velocity U = 10 m/s for the 22-foil-2 electrode pair

5.2 Numerical Results for Cascade Tests

Numerical results were obtained for all four cascade test cases and, as with the flat plate experimental results, the model showed generally good agreement. Figure 5.2.1 below shows a comparison of the numerical and measured results for the case of a stagger angle of 25°, angle of attack of 6°, and free-stream velocity magnitude of 10 m/s.

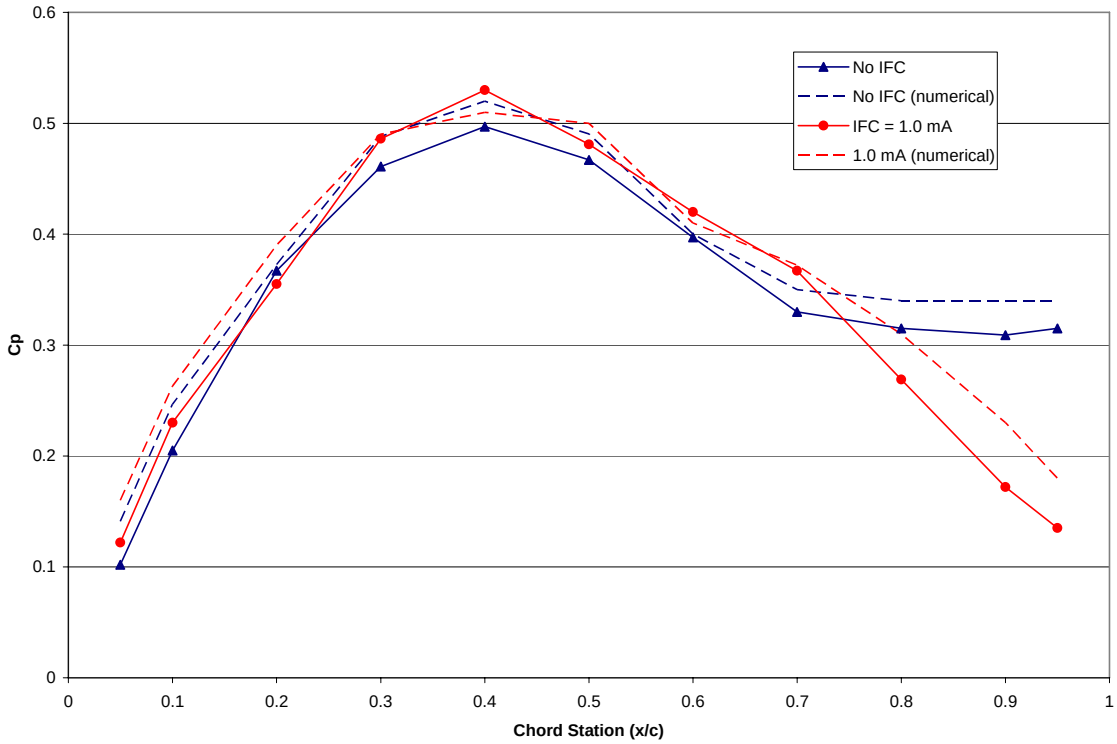

Figure 5.2.1 Numerical and experimental comparison for cascade static tap data: $\xi = 25^{o}$, $\alpha^{*} = 6°$, U = 10 m/s

Although the numerical results are not in exact agreement with the experimental data, the model clearly demonstrates the ability to correctly predict the trends of the flow behavior, with and without ion flow control. The computational model showed trailing edge separated flow for the case of no ion flow control. When the ion-induced body force was added to the computational setup the model accurately predicted reattachment of the separated flow at the blade's trailing edge.

Chapter 6

Summary, Conclusions and Recommendations

A foundation for ion flow control research at the Virginia Tech Turbo Lab has been developed. The effect of a positive, DC corona discharge on the boundary layer profile along a flat plate has been tested at various free-stream velocities and discharge current settings. Also, the corona discharge has been tested in a low-speed compressor cascade to determine its effect on preventing separated flow for various cascade test setups. A computational model has been developed using the commercial CFD software Fluent. This model simulates ion flow control as a body force applied to the flow through user-defined functions.

The corona discharge has shown the ability to increase near-wall velocities and reduce the thickness of the boundary layer for flow over a flat plate. At free-stream velocity magnitudes of 2.5, 5, and 7.5 m/s, the discharge accelerates the flow to velocities above the free-stream magnitude. At higher free-stream values (10 m/s), the flow acceleration is less intense; however, the boundary layer thickness is reduced by approximately 50%.

Ion flow control successfully prevented trailing edge separation in a compressor cascade for angles of attack of 6° and 12°. The flow control scheme was not, however, able to prevent leading edge separation for angle of attack equal to 12°. In cascade experiments, ion flow control performance improved for higher free-stream velocity magnitudes. This is considered to be due to the increase in the energy of the higher velocity free-stream flow, which contributed to less severe separation.

The ion flow control model was able to accurately predict flow behavior for both the flat plate and the cascade experiments. The numerical model was able to simulate the boundary layer velocity profiles for flat plate tests with good accuracy. The model correctly predicted the height above the plate surface at which the maximum velocity was

reached as well as the boundary layer thickness for the range of free-stream velocity magnitudes tested. The model was also able to predict the flow behavior over a compressor blade. While the numerical results were not in exact agreement with the experimental results, the model was clearly able to show the trends of separated and reattached flow over the blade surface.

The conclusions reached in this study are summarized below:

- The electrode configuration consisting of an AWG 22 copper wire positive lead and a strip of copper foil as a negative lead provided the greatest discharge current at lower levels of power consumption.
- The copper foil strip was the best ion receptor of the electrode types examined.
- A downstream electrode with a negative potential provided a preferred path for the positive ions created by the corona discharge upstream and eliminated charge losses to the surrounding; therefore, larger current values were obtained for a given local electric field strength.
- The ion-induced body force seemed to be wholly determined by the discharge current and the electric field required to generate that current value.
- For a free-stream velocity magnitude of 2.5 m/s, the boundary layer thickness was increased; however, the opposite was true for free-stream magnitudes of 5, 7.5, and 10 m/s.
- Varying electrode geometry did not affect the nature of the boundary layer velocity profile.
- The force produced by the corona discharge seemed to act tangentially to the flow and was greatest close to the surface.
- To prevent separated behavior over a compressor cascade blade, the electrode pair should be placed before the separation point.

The results reported herein provide a foundation that may be used to continue the investigation of ion flow control. In order to perform tests at higher free-stream velocities, the single dielectric barrier discharge (SDBD) should be explored. This type

of plasma actuator, discussed in the introductory chapter of this thesis, allows for a greater ion-induced force to be imparted to the flow. Pulsed-DC excitation should be examined as a means of increasing the efficiency of the SDBD actuator. Micro- or nanosecond pulse widths at pulse frequencies of 100 Hz and greater have shown the ability to control boundary layer separation, lift and drag coefficients, and reduce noise over a Mach number range of 0.05 to 0.85 [9].

The effect of ion flow control on wake reduction and total pressure loss coefficient should be examined for continued experiments. There should be a reduction in wake thickness in cases where separated flow behavior has been prevented; however, this effect should be quantified with pressure measurement rakes. By characterizing the flow upstream and downstream of the compressor blade, the total pressure loss coefficient can be calculated and the effect of ion flow control on cascade performance can be measured.

The computational model for ion flow control developed in this study can be used for the design of new experiments. While there is debate over the physical mechanism responsible for the force due to pulsed-DC plasma actuation [9, 15], it has been shown that a source term applied in an unsteady, pulsed manner can produce momentum transfer in the near-wall region that prevents boundary layer separation [16]. Some researchers have expressed the opinion that the main mechanism for flow reattachment is the "energy transfer to and heating of the near-surface gas layer" [9]. If initial numerical results prove to be inaccurate and the heat release of the plasma discharge appears to play a role in the generation of the ion-induced force, the computational model has the capability of simulating the thermalization of the near-wall region. The simple solution is the creation of a new UDF that can be used in tandem with the previously developed function. This new function could prescribe a heat flux source that acts through the SDBD surface to heat the "near-surface gas layer" [9]. Infrared imaging should be used to measure the temperature generated by the SDBD actuators during plasma characteristic tests. These results can then be used in calibrating the new UDF to more accurately model ion flow control.

References

[1] Howatson, A.M. (1976). *An Introduction to Gas Discharges.* New York: Pergamon Press.

[2] Raizer, Yuri P. (1997). *Gas Discharge Physics.* New York: Springer

[3] Cobine, James Dillon. (1941). *Gaseous Conductors.* New York: McGraw-Hill Book Company, Inc.

[4] Leger, L., Moreau, E., Touchard, G. (2002) Effect of a DC Corona Electrical Discharge on the Airflow Along a Flat Plate. *IEEE Transactions,* 38(6), 1478-1485.

[5] Leger, L., Moreau, E., Touchard, G. "Electrohydrodynamic airflow control along a flat plate by a DC surface corona discharge – Velocity profile and wall pressure measurements," presented at the 1st AIAA Flow Control Conference, St. Louis, MO, June 24-26, 2002, Paper 2002-2833.

[6] Walker, M.L.R. (2005) "Electrostatic Propulsion Investigation," Georgia Tech Institute of Technology High-Power Electric Propulsion Laboratory

[7] Rickard, M., Dunn-Rankin, D., Weinberg, F., Carleton, F. "Maximizing ion-driven gas flows," *J. Electrostatics,* vol. 64, pp. 368-376, 2006.

[8] Seraudie, A., Aubert, E., Naude, N., Cambronne, J.P. "Effect of plasma actuators on a flat plate laminar boundary layer in subsonic conditions," presented at the 3rd AIAA Flow Control Conference, San Francisco, CA, June 5-9, 2006, Paper 2006-3350

[9] Roupassov, D.V., Nikipelov, A.A., Nudnova, M.M., Starikovskii, A.Yu. "Boundary Layer Separation Control by Nanosecond Plasma Actuator," presented at 44th AIAA Joint Propulsion Conference, Hartford, CT, July 21-23, 2008, Paper 2008-5067.

[10] Wall, J.D., Boxx, I.C., Rivir, R.B., Franke, M.E. "Effects of Pulsed-DC Discharge Plasma Actuators in a Separated Low Pressure Turbine Boundary Layer," presented at 45th AIAA Aerospace Sciences Meeting, Reno, NV, January 8-11, 2007, Paper 2007-942.

[11] Corke, T.C., Post, M.L. "Overview of Plasma Flow Control: Concepts, Optimization, and Applications," AIAA Paper 2005-4630

[12] Huang, J., Corke, T.C., Thomas, F.O. "Plasma Actuators for Separation Control of Low Pressure Turbine Blades," presented at 41st AIAA Aerospace Sciences Meeting, Reno, NV, January 6-9, 2003, Paper 2003-1027.

[13] Rivir, R., White, A., Carter, C., Ganguly B. "AC and Pulsed Plasma Flow Control," presented at 42nd AIAA Aerospace Sciences Meeting, Reno, NV, January 5-8, 2004, Paper 2004-847.

[14] El-Khabiry, S., Colver, G.M. "Drag reduction by dc corona discharge along an electrically conductive flat plate for small Reynolds number flow," *Phys. Fluids,* 9 (3), pp. 587-599, Mar. 1997.

[15] Boeuf, J.P., Lagmich, Y., Callegari, Th., Pitchford, L.C. "EHD Force in Dielectric Barrier Discharges Parametric Study and Influence of Negative Ions," presented at 45th AIAA Aerospace Sciences Meeting, Reno, NV, January 8-11, 2007, Paper 2007-183.

[16] Rizzetta, D.P., Visbal, M.R. “Numerical Investigation of Plasma-Based Flow Control for a Transitional Highly-Loaded Low-Pressure Turbine,” presented at 45th AIAA Aerospace Sciences Meeting, Reno, NV, January 8-11, 2007, Paper 2007-938.

[17] Perry, Michael A., Jr., “The Effect of Free stream Turbulence on Separation at Low Reynolds Numbers in a Compressor Cascade,” M.S. Thesis, Mechanical Engineering, VPI & SU, 2007.

[18] Walters, D. K., and Leylek, J. H., 2004, "A New Model for Boundary-Layer Transition Using a Single-Point RANS Approach,*"ASME J. Turbomach*., 126, pp. 193-202

[19] Walters, D. K., and Leylek, J. H., 2005, “Computational Fluid Dynamics Study of Wake-Induced Transition on a Compressor-Like Flat Plate,” *ASME J. Turbomach*., 127, pp. 52-63

[20] Sanders, D., “Predicting Separation and Transitional Flow in Turbine Blades at Low Reynolds Numbers,” IGTI 2008, Paper GT2008-50283

[21] Szirtes, T. (2007). *Applied Dimensional Analysis and Modeling.* New York: Butterworth-Heinemann.

[22] Minick, A., and Cousins, W. T., personal communication on internal Pratt & Whitney work, 2007-2009.

Appendix A

Non-Dimensional Analysis of Ion Flow Control

The ion flow control design space was investigated through a dimensional analysis of the characteristic variables of the phenomenon. In order to carry out this analysis, the text *Applied Dimensional Analysis and Modeling* by Thomas Szirtes was used [21]. This resource provided a guide for determining the characteristics that apply to a physical quantity, in our case the ion-induced plasma force. Szirtes method utilized a dimensional matrix that reduced the number of dimensional variables to a group of π terms. This method is similar in nature to the Buckingham-π Theorem. A benefit of Szirtes method was its ability to determine dimensionally irrelevant variables. Szirtes defined an irrelevant variable as one that "*cannot* be part of any relation among the variables *solely* because of its dimension" [21]. Once identified, these independent variables could be removed from the list of possible characteristic variables. In some cases, the deletion of an irrelevant variable would lead to the appearance of new irrelevant variables. As each was removed from the dimensional matrix another irrelevant variable would be identified. Szirtes defined this circumstance as the "cascading effect." The cascading effect was beneficial, however, because it led to the discovery that a relevant variable had been omitted from the original set of independent variables. If an attempt to develop a set of π terms led to the appearance of the cascading effect, the list of independent variables was reevaluated. This was the iterative process used to develop sets of π terms until a group was discovered that adequately represented the ion flow control design space.

In order to use the Szirtes method, the independent variables that govern the plasma actuation process must be identified. As a first attempt, the following parameters were selected:

Fp – plasma-induced force
V – voltage

Ip – ionization potential

MW – molecular weight

R – effective radius of electrode (electrode geometric parameter)

s – electrode spacing

T – temperature

P – pressure

This initial attempt proved to be a failure because the voltage was identified as an irrelevant variable, which cannot be true for this investigation. Further literature review led to the discovery of the electrostatic approximation; that is the force a local electric field exerts on a charged particle within its domain. Therefore, the variable q was added to represent the charge magnitude of a positive ion. Additional changes made to the independent variable set were the combining if the pressure, temperature, and molecular weight to give the density of the fluid. Also the dynamic and kinematic viscosities were added to the set. In order to further include the dynamic effects of the free-stream air, the velocity, U, was added to the group. The last variable included in the dimensional set was frequency. This was meant to incorporate either the shedding frequency for the flow application or the pulse frequency of the plasma actuator into the defining characteristics of the physical phenomenon. The complete variable set is shown below.

Fp – force on the fluid

R – effective radius of electrode (electrode geometric parameter)

s – electrode spacing

U – free-stream velocity

V – voltage

Ip – ionization potential

q – charge of an electron

ρ – free-stream density

μ – dynamic viscosity

ν – kinematic viscosity

MW – molecular weight

f – frequency

The evolution of the π terms is illustrated below:

Original group of non-dimensional parameters:

$$\Pi_1 = \frac{F_p}{R^2 \rho U^2} \qquad \Pi_2 = \frac{s}{R} \qquad \Pi_3 = \frac{Vq}{R^3 \rho U^2} \qquad \Pi_4 = \frac{I_p}{R^3 \rho U^2}$$

New set of ND terms with addition of viscosity to variable set:

$$\Pi_1 = \frac{\rho F_p}{\mu^2} \qquad \Pi_2 = \frac{\rho U s}{\mu} \qquad \Pi_3 = \frac{\rho^2 V q U}{\mu^3} \qquad \Pi_4 = \frac{I_p \rho^2 U}{\mu^3} \qquad \Pi_5 = \frac{\rho U R}{\mu}$$

The next iteration of terms substituted ν instead of μ and ρ:

$$\Pi_1 = \frac{F_p R}{Vq} \qquad \Pi_2 = \frac{s}{R} \qquad \Pi_3 = \frac{I_p}{Vq} \qquad \Pi_4 = \frac{UR}{\nu}$$

With the addition of molecular weight to incorporate proper dimension of ionization potential, the terms become:

$$\Pi_1 = \frac{F_p R}{Vq} \qquad \Pi_2 = \frac{s}{R} \qquad \Pi_3 = \frac{I_p}{U^2 MW} \qquad \Pi_4 = \frac{UR}{\nu}$$

The inclusion of frequency (as in the shedding or pulse frequency) leads to the final set of non-dimensional terms

$$\Pi_1 = \frac{F_p s}{Vq} \qquad \Pi_2 = \frac{R}{s} \qquad \Pi_3 = \frac{I_p}{U^2 MW} \qquad \Pi_4 = \frac{Us}{\nu} \qquad \Pi_5 = \frac{fs}{U}$$

The final set of π terms included two classical non-dimensional numbers. Both the Reynolds and Strouhal numbers were identified as important parameters that characterized ion flow control. This is supported by current research that examined the effects of pulse frequency on increasing the efficiency of plasma actuators. Matching the pulse rate to the shedding frequency allows actuator operation at a Strouhal number of one, which has been proven as a means of increasing the effect of ion flow control. The first π term is merely the electrostatic approximation non-dimensionalized. The second term is a geometric ratio that defines the design of the emitter/receptor pair. The emitting radius and spacing of the electrodes is encompassed in this term. It can be used to further classify new configurations of electrodes with varying geometry. There were initial plans to investigate seeding the flow with a gas that possessed a lower ionization potential than air. The idea being that a greater number of positive ions would be produced and therefore the magnitude of the ion-induced force would be increased. The third π term includes the ionization potential and molecular weight; the variables which characterize this flow seeding theory. The idea was abandoned after further literature review and initial experiments were conducted. However, this third term may be relevant at higher free-stream velocity magnitudes. The term does contain the free-stream velocity variable, U, and the change in the physical properties of the air at higher speeds could affect the ion-induced force. This final set of five π terms was used to design experiments conducted in this study and investigate the benefits of ion flow control.

Appendix B

Results for Computational Model Validation

This appendix contains all of the plots comparing the experimental results to those of the numerical model. Rather than cluttering the Results section of Chapter 5, these results are presented here. The results are organized in a similar manner to the provided plots and discussion in the body of the document. The validation of flat plate tests for each electrode configuration is shown first, followed by data comparisons of the cascade test results.

B.1 Flat Plate Boundary Layer Velocity Profile Validation

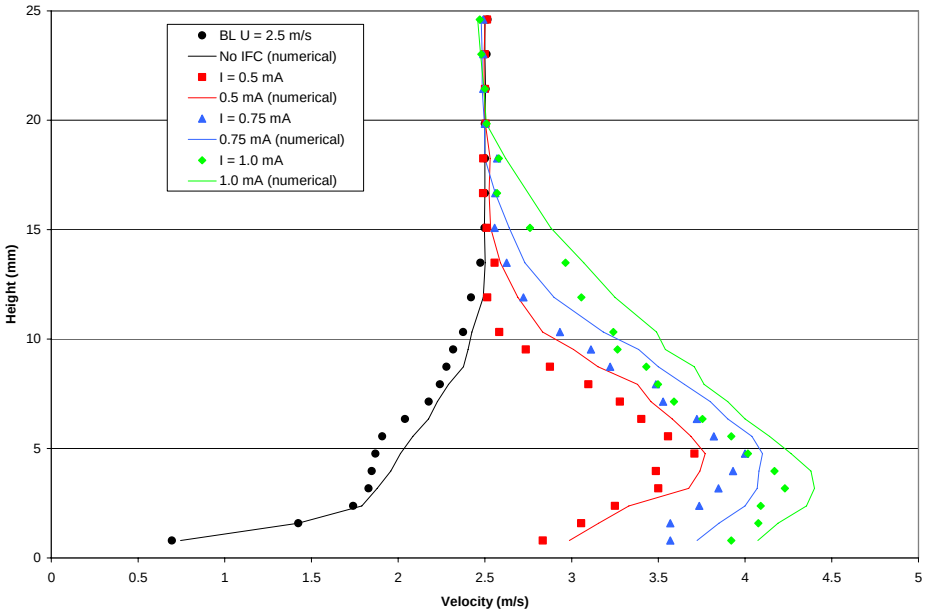

Figure B.1 Numerical and experimental comparison for boundary layer velocity profiles at free-stream velocity U = 2.5 m/s for the 34-22-3 electrode pair

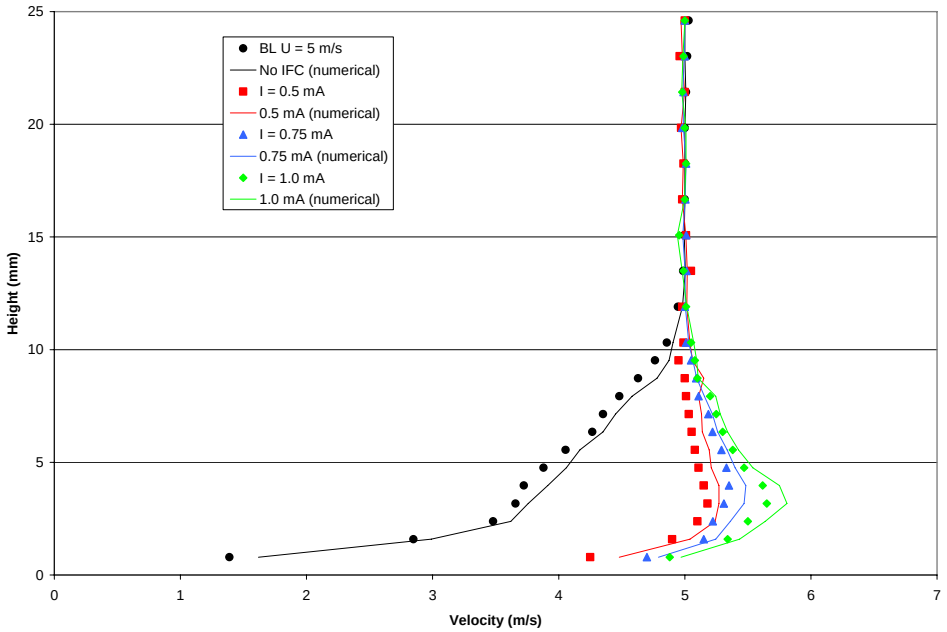

Figure B.2 Numerical and experimental comparison for boundary layer velocity profiles at free-stream velocity U = 5 m/s for the 34-22-3 electrode pair

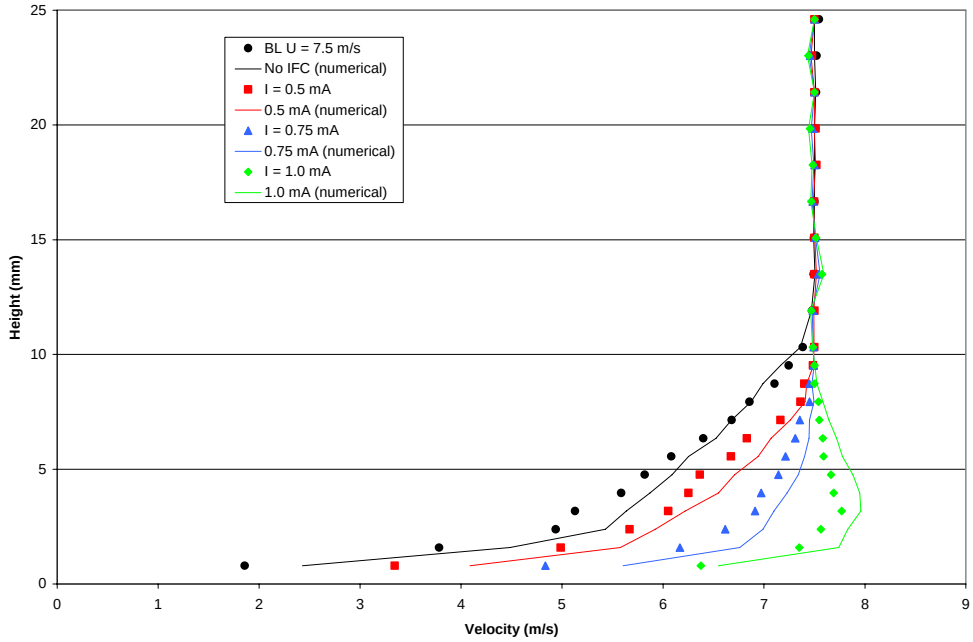

Figure B.3 Numerical and experimental comparison for boundary layer velocity profiles at free-stream velocity U = 7.5 m/s for the 34-22-3 electrode pair

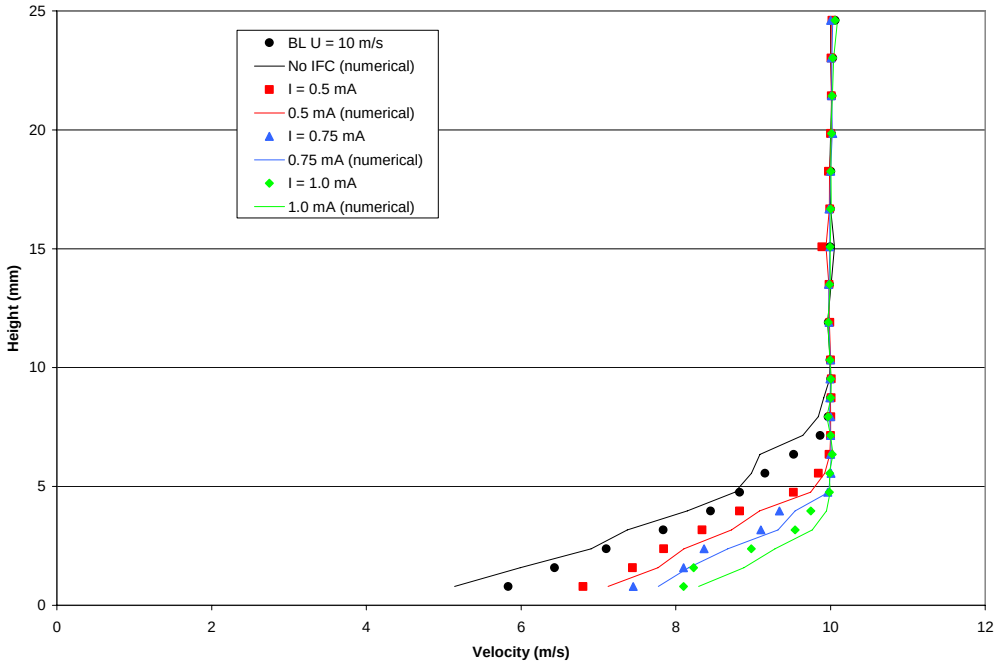

Figure B.4 Numerical and experimental comparison for boundary layer velocity profiles at free-stream velocity U = 10 m/s for the 34-22-3 electrode pair

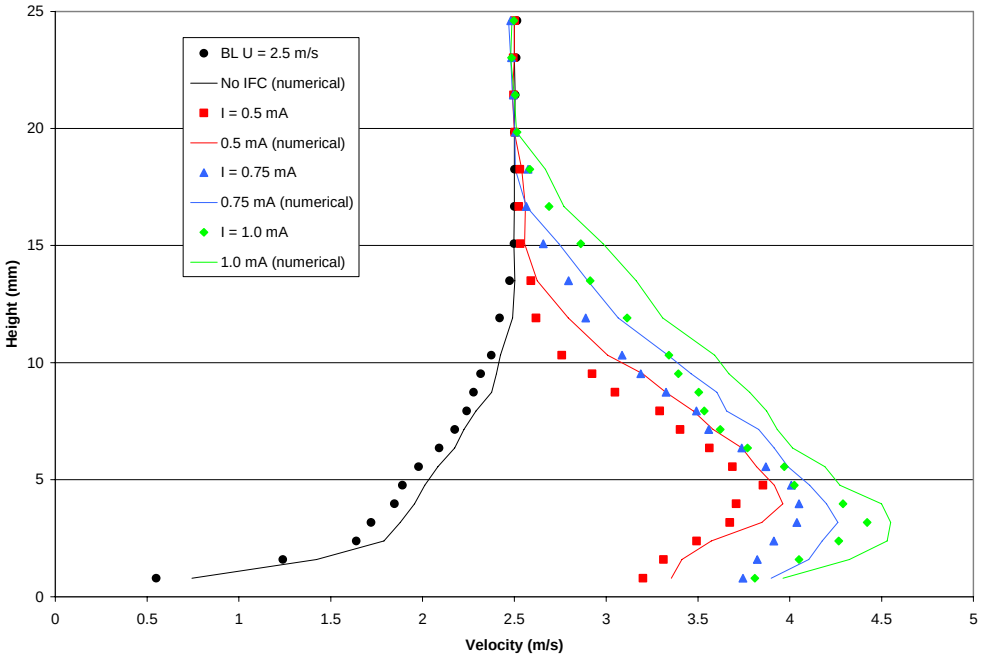

Figure B.5 Numerical and experimental comparison for boundary layer velocity profiles at free-stream velocity U = 2.5 m/s for the 22-foil-2 electrode pair

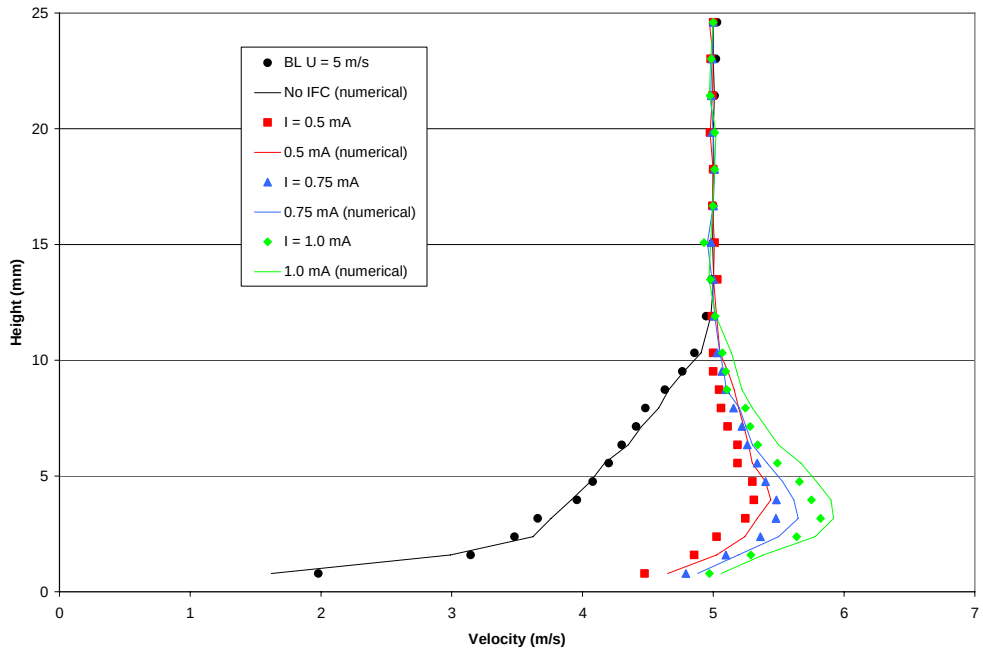

Figure B.6 Numerical and experimental comparison for boundary layer velocity profiles at free-stream velocity U = 5 m/s for the 22-foil-2 electrode pair

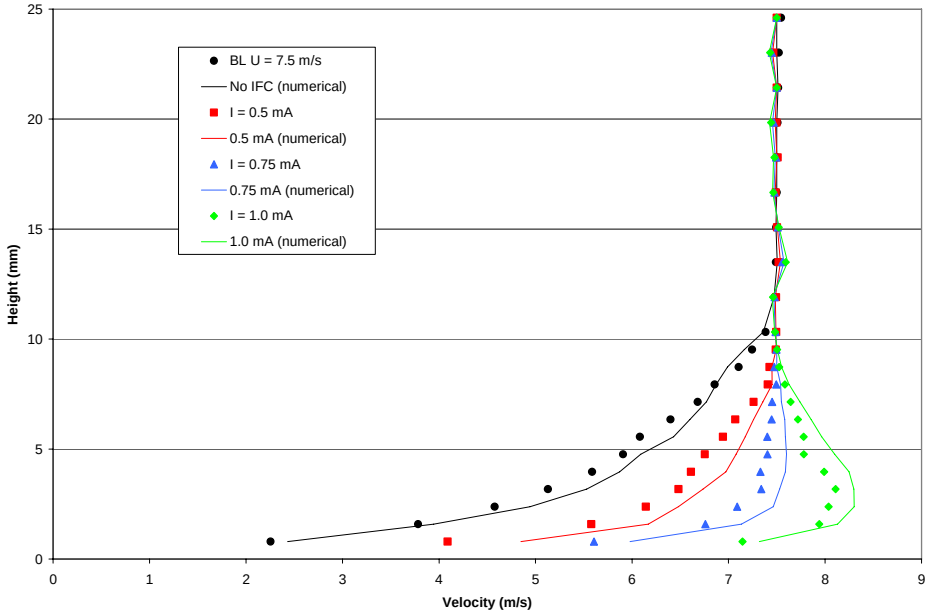

Figure B.7 Numerical and experimental comparison for boundary layer velocity profiles at free-stream velocity U = 7.5 m/s for the 22-foil-2 electrode pair

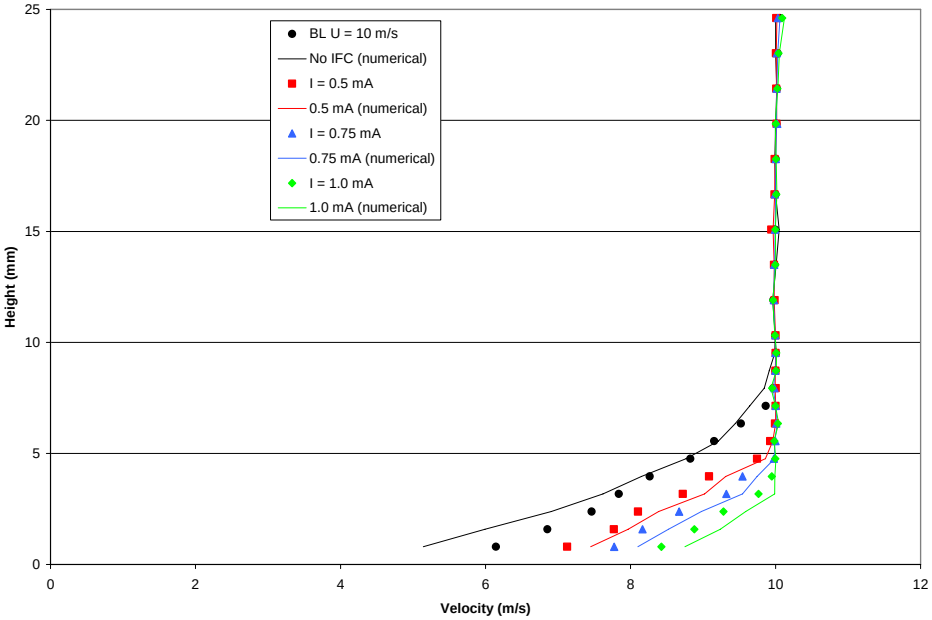

Figure B.8 Numerical and experimental comparison for boundary layer velocity profiles at free-stream velocity U = 10 m/s for the 22-foil-2 electrode pair

B.2 Cascade Static Tap Validation

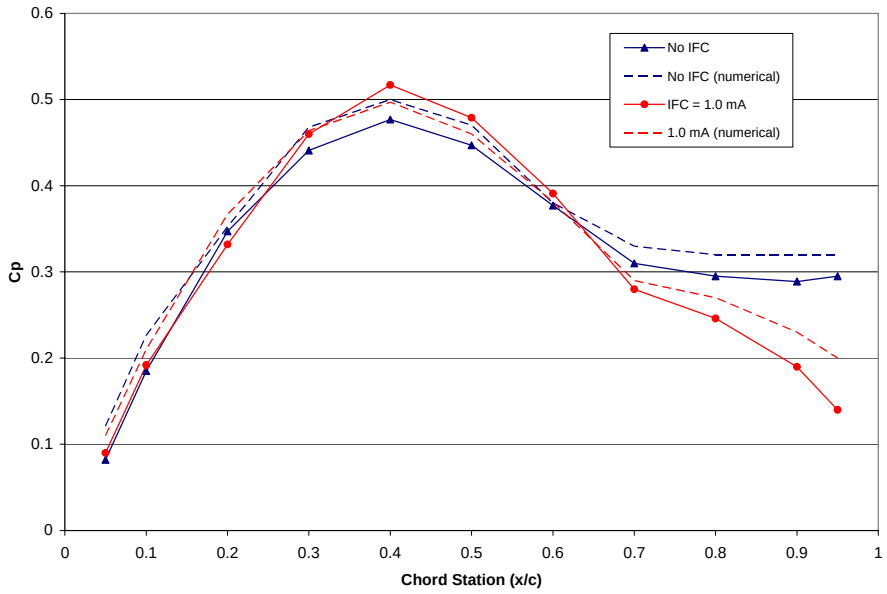

Figure B.9 Numerical and experimental comparison for cascade static tap data: $\xi = 25º$, $\alpha^* = 6°$, U = 5 m/s

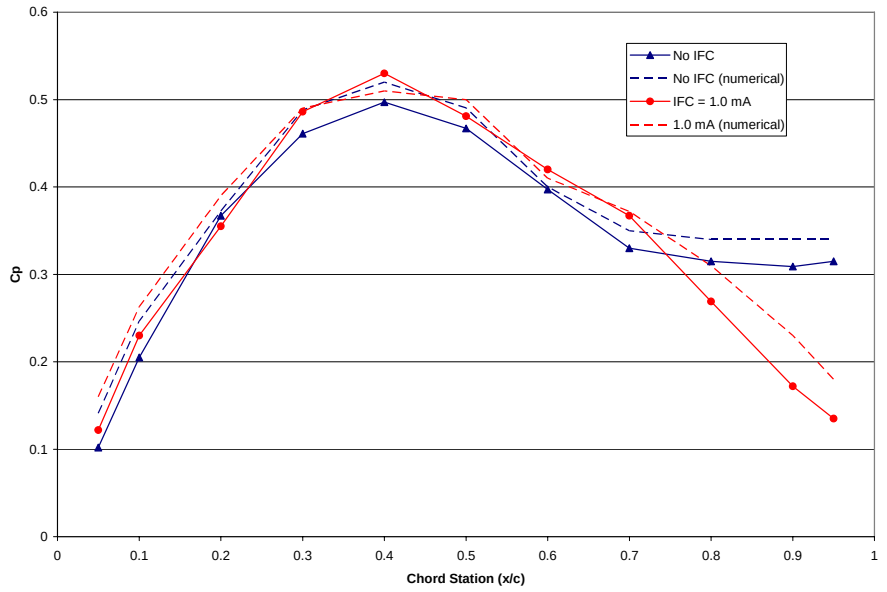

Figure B.10 Numerical and experimental comparison for cascade static tap data: $\xi = 25º$, $\alpha^* = 6°$, U = 10 m/s

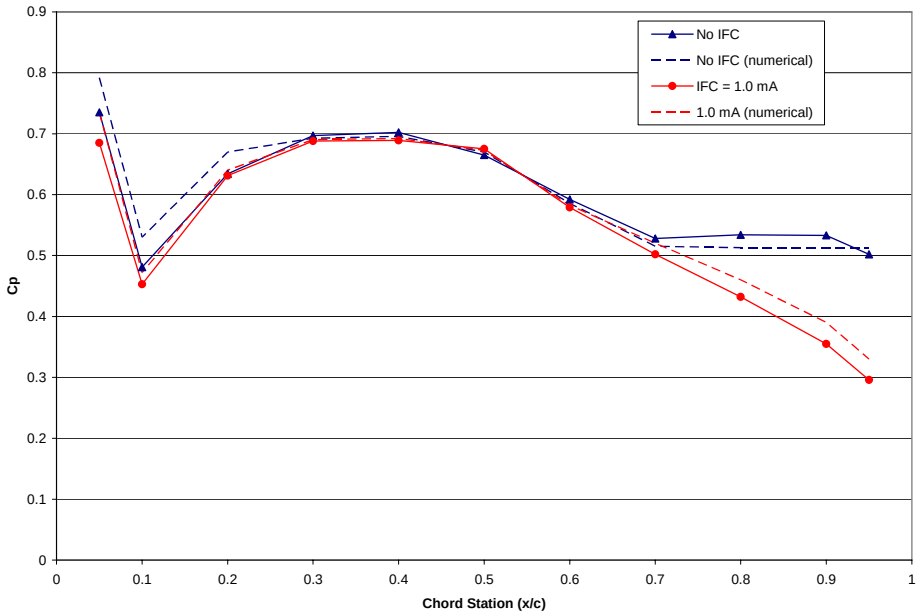

Figure B.11 Numerical and experimental comparison for cascade static tap data: $\xi = 25^{\circ}$, $\alpha^* = 12°$, U = 5 m/s

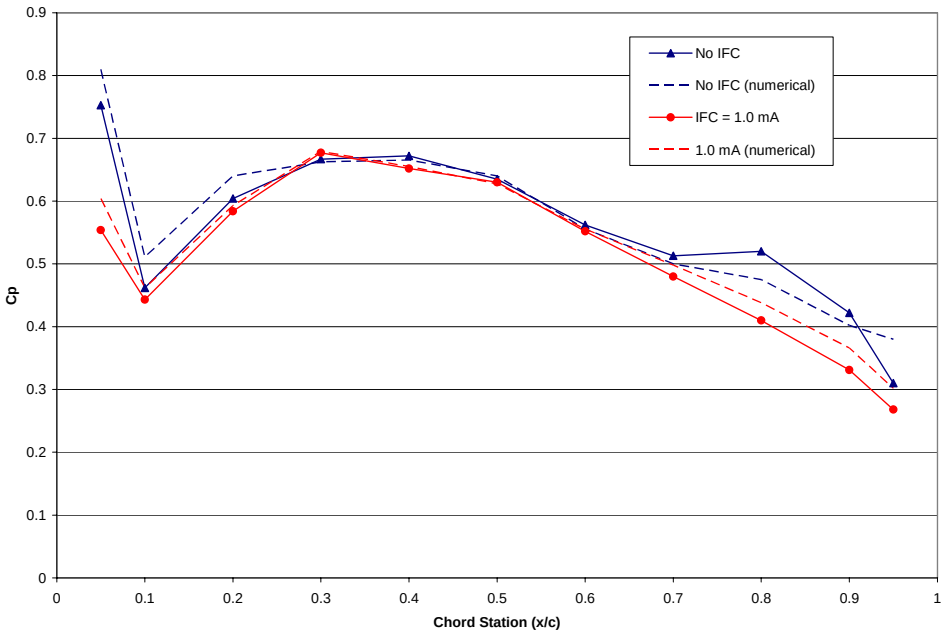

Figure B.12 Numerical and experimental comparison for cascade static tap data: $\xi = 25^{\circ}$, $\alpha^* = 12°$, U = 10 m/s

Appendix C

Vendor List

This appendix contains a list of vendors that supplied various products, equipment, and instrumentation used in this study. Where applicable, contact information is provided to help in obtaining certain products that may be used in further studies.

Power Supplies

Glassman High Voltage Power Supply Model FC30P4

Pacific Instruments High Voltage Power Supply Model 204-10

Dielectric Sheet

Kapton® 100 CR and 400 HN dielectric film

Produced by DuPont – specifications and free samples available at the company website

Smoke Visualization Equipment and Supplies

ELIMINATOR EF-1000 Fog Machine

Purchased from www.prolightingsupplies.com

Website can be used to purchase smoke machine fluid

Composite Component Casting Supplies

Alumilite molding and casting resins

Purchased from www.alumilite.com

Website can be used to purchase mold making silicon and casting resin

Pressure Transducers

Setra Model 264 Very Low Differential Pressure Transducers

Ranges of the transducers were 2.5" H_2O, 0.5" H_2O, and 0.1" H_2O